

Alluvial architecture of mid-channel fluvial-tidal barforms: the mesotidal Lower Columbia River, OR/WA, USA

Prokocki, E.W.^{1,*}, Best, J.L.^{1,2}, Ashworth, P.J.³, Sambrook Smith, G.H.⁴, Nicholas, A.P.⁵, Parsons, D.R.⁶, Simpson, C.J.⁷

¹Department of Geology, University of Illinois, 1301 West Green Street, Urbana, IL 61801, USA
*now at: Jackson School of Geosciences, 2305 Speedway Stop C1160, Austin, TX 78712, USA
(Email: ewaschle2@gmail.com)

²Departments of Geography & GIS, Mechanical Science and Engineering, and Ven Te Chow Hydrosystems Laboratory, University of Illinois, 1301 West Green Street, Urbana, IL 61801, USA

³Division of Geography and Geology, School of Environment and Technology, University of Brighton, Brighton, Sussex BN2 4GJ, UK

⁴School of Geography, Earth, Environmental Sciences, University of Birmingham, Edgbaston, Birmingham, B15 2TT, UK

⁵Department of Geography, College of Life and Environmental Sciences, University of Exeter, EX4 4RJ, UK

⁶Department of Geography, Environment and Earth Sciences, Faculty of Science and Engineering, University of Hull, Hull, HU6 7RX, UK

⁷Fulcrum Graphic Communications Inc., Airdrie, Alberta, Canada

Short title: Fluvio-tidal barform architecture and sedimentology

ABSTRACT

Barforms of mesotidal to macrotidal fluvial-tidal transitions (FTTs), regardless of fluvial-discharge, are currently thought to display a sedimentary architecture containing tidal signatures.

Due to the scarcity of observations from modern mesotidal FTTs, especially those of multi-channelled large-rivers (mean annual discharge $\geq 7,000 \text{ m}^3\text{s}^{-1}$, and peak discharges $\geq 15,000 \text{ m}^3\text{s}^{-1}$)

with mid-channel bars, this concept remains unproven. The present study analyses data produced by a combination of high-resolution ground penetrating radar (GPR) and coupled shallow vibracores ($< 5\text{m}$ depth), collected from modern FTT mid-channel bars of the mesotidal multi-channelled Lower Columbia River (LCR), WA/OR, USA, which experiences peak discharges $\geq 18,000 \text{ m}^3\text{s}^{-1}$. These data were used alongside time-sequenced aerial imagery to

characterise the spatio-temporal sedimentological evolution of these barforms in singular- or combined- flows consisting of river-, tidal-, and/or wind-wave oscillatory-, current components operating in unique FTT regimes. Results indicate that ~ 75% of the LCR FTT produces braid-bars with basal to bar-top sedimentological architectures that are indistinguishable from fluvial-only braid-bars recorded in the literature. Barform stratal characteristics within the FTTs of mesotidal large-rivers are therefore more likely to be dominated by downstream-oriented currents. Furthermore, a new style of low-angle ($< 5^\circ$) Inclined Heterolithic Stratification (IHS) found in bar-top accretion-sets within upper-mixed tidal-fluvial regime (MTFR) braid-bars is observed. This common stratification is created by combined-flows characterised by intrabasinal wind-wave oscillatory-currents and bidirectional tidal-currents. This IHS marks the initial downstream FTT crossover point from LCR up-dip fully-fluvial braid-bar architectures, to those possessing bar-top facies produced by the hydraulic-sedimentation response of combined intrabasinal wind-wave and tidal influence. When preserved, this form of mid-channel bar IHS provides a unique sedimentological signature of multi-channelled FTTs that possess an open-water lower basin with intrabasinal wind-waves.

Keywords: Lower Columbia River, fluvial-tidal bars, intrabasinal wind-waves, Inclined Heterolithic Stratification

(A) INTRODUCTION

Fluvial-tidal transitions (FTTs), or fluvial-tidal zones (van den Berg *et al.*, 2007), are one of the most complex multi- to single- thread channelized settings on Earth (Dalrymple & Choi, 2007). Depending on channel-bed slope and tidal range, FTTs may extend 10s to 100s of river

kilometres (rkm) landward from river mouths to the landward most point of measurable tidally-induced variations of the low-river stage water surface, or tidal-limit (Dalrymple & Choi, 2007; Hoitink & Jay, 2016). Thus, FTTs span several unique settings from lower estuaries, or deltas, where salt-wedge intrusion occurs, to the brackish-water upper estuary, or delta, and through the freshwater tidal river reach (cf. Dalrymple & Choi, 2007; Hoitink & Jay, 2016). FTTs are combined-flow environments characterized by the interplay between bidirectional tidal-flows, unidirectional river-currents, oceanic to intrabasinal wind-waves, and density-driven vorticity generated by saltwater intrusion (Dalrymple & Choi, 2007). By evaluating either the mean ratio of hypothesized (Dalrymple et al., 2015), or measured (Jay *et al.*, 1990; Losada *et al.*, 2017), tidal- vs fluvial- energy input, three general hydraulic zones describe FTTs (cf. Jay *et al.*, 1990; Hoitink & Jay, 2016; Jablonski & Dalrymple, 2016): i) marine to tidally-dominated lower estuary, or delta, ii) tidally-dominated, fluvially-influenced, or mixed tidal-fluvial regime (upper estuary, or delta, to lower tidal river reach), and iii) fluvially-dominated, tidally-influenced regime (mid- to upper- tidal river reach). The longitudinal boundaries of these regimes, however, fluctuate in space and time due to the interactions between spring to neap tidal-cycles and varying river-stages (Dalrymple & Choi, 2007; Dalrymple *et al.*, 2015). This classification scheme does, however, exclude the effects of oceanic-waves within lower FTTs and intrabasinal wind-waves in mid- to upper- FTTs, which can be important hydraulic constituents in particular settings (cf. Chaumillon *et al.*, 2008; Peterson *et al.*, 2014; Prokocki *et al.*, 2015).

Point-bars or mid-channel bars (Hubbard *et al.*, 2011; Jablonski & Dalrymple, 2016; Leuven *et al.*, 2016; van de Lageweg & Feldman, 2018) may characterize FTTs, and their presence depends on whether the system is multi-channelled or single-threaded (Seminara *et al.*, 2001). Due to the interplay between the dominant and subordinate fluvial-tidal currents, the

sedimentology of FTT barforms is likely more complex than unidirectional-current fluvial bars (Dalrymple & Choi, 2007; van den Berg *et al.*, 2007; Martinius & van den Berg, 2011; van de Lageweg & Feldman, 2018). A widely adopted fluvial-tidal barform model suggests that in the downstream-direction there is a tendency for FTT barform accretion-sets to develop Inclined Heterolithic Stratification (IHS; Thomas *et al.*, 1987), where enhanced fine-grained deposition occurs during tidal-slackwater intervals, and near the turbidity-maximum (TM; Fig. 1). This model, however, is limited in four respects. First, its foundation rests upon a small number of modern studies (e.g., Smith 1987, 1989; Choi *et al.*, 2004; Dalrymple & Choi, 2007; Dalrymple *et al.*, 2012; Johnson & Dashtgard, 2014), whilst relying heavily on observations from ancient fluvial-tidal settings (e.g., Hubbard *et al.*, 2011; Fustic *et al.*, 2012; Feldman & Demko, 2015; Martinius *et al.*, 2015; Jablonski & Dalrymple, 2016), where the planform geometry, and hydraulic initial and boundary conditions, are not well-constrained. Secondly, it implies that IHS is strongly related to tidal-processes, and deemphasises the potential importance of fluvial and wind-wave processes (Smith *et al.*, 2009, 2011; Durkin *et al.*, 2015; Moreton & Carter, 2015) in producing IHS. Thirdly, it is conditioned upon single-thread FTTs with point-bars, and thus it is unknown whether the IHS model applies to multi-channelled FTTs with mid-channel bars. Lastly, it portrays IHS trends from a longitudinal-viewpoint (upstream to downstream), and does not consider lateral variations.

Establishing whether contemporary FTT bars possess a sedimentological signature that can be unambiguously distinguished from purely marine and fluvial deposits is important for several reasons. Within sequence stratigraphic models, FTTs mark the landward extent of transgression, and represent the basal flooding surfaces of highstand successions (Dalrymple *et al.*, 1992; Shanley *et al.*, 1992; Boyd *et al.*, 2006; Dalrymple & Choi, 2007). Knowledge of FTT

stratal architecture is also beneficial to hydrocarbon exploration and production. For example, the Cretaceous bitumen-rich McMurray Formation, Alberta, Canada (Hein, 2015), is commonly interpreted as being constructed from FTT barform strata (Smith, 1988, 1989; Wightman & Pemberton, 1997; Wightman *et al.*, 1997; Hubbard *et al.*, 2011; Fustic *et al.*, 2012; Feldman & Demko, 2015; Martinius *et al.*, 2015; Jablonski & Dalrymple, 2016), but fully-fluvial McMurray Formation barform depositional models have also been proposed (cf. Moreton & Carter, 2015). Modern FTT barforms have thus received a lot of recent attention (Smith 1987, 1989; Smith *et al.*, 2009; Choi, 2010; Sisulak & Dashtgard, 2012; Choi *et al.*, 2013; Johnson & Dashtgard, 2014; Carling *et al.*, 2015; Prokocki *et al.*, 2015; Leuven *et al.*, 2016) in order to establish how fluvial-tidal processes alter their morphology and alluvial architecture. Most sedimentological observations from modern FTTs, however, are restricted to bed-scale trenches and cores (e.g., Dalrymple & Rhodes, 1995; Choi *et al.*, 2004; van den Berg *et al.*, 2007; Baker *et al.*, 2010; Martinius & van den Berg, 2011; Sisulak & Dashtgard, 2012; Peterson *et al.*, 2014; Carling *et al.*, 2015; Prokocki *et al.*, 2015; Ghinassi *et al.*, 2018), whilst seismic data of bar-scale architecture is scarce, limited in its spatial resolution and confined to individual sandbanks, or sandbars (Chaumillon *et al.*, 2008, 2013). Thus, while abundant bar-scale seismic data exists for ancient tide-dominated offshore deposits (Berné *et al.*, 2002) and fluvio-tidal systems (Hubbard *et al.*, 2011; Reijenstein *et al.*, 2011), comparable data from modern FTT barforms is limited.

To address this data deficiency, the present study presents an integrated ground penetrating radar (GPR) and shallow (< 5m depth) vibrocore dataset collected in 2011 and 2013 from FTT mid-channel bars of the mesotidal sand-bed, Lower Columbia River (LCR), USA (Fig. 2A-D). Three primary questions are addressed herein:

- 1) What is the sedimentologic architecture of large-river mid-channel bars within the mixed tidal-fluvial to fluvially-dominated, tidally-influenced FTT hydraulic regimes?
- 2) How does potential IHS within FTT mid-channel bar alluvial successions relate to: i) bar migration rates and patterns, and ii) varying contributions of combined-flow currents and associated depositional processes?
- 3) How similar, or different, is the sedimentary architecture of large-river FTT mid-channel bars relative to fluvial braid-bars?

(A) STUDY REACH: LOWER COLUMBIA RIVER FTT

(B) Modern fluvial-tidal characteristics

From the late 1800s to present, human-intervention within the Columbia River drainage basin has disrupted water and sediment supplies via irrigation depletion and dam closures, main navigation channel dredging and sand-mining, the installation of upriver permeable pile-dikes along the navigation channel, and jetty and dike construction at its mouth (Sherwood *et al.*, 1990; Gelfenbaum *et al.*, 1999; Jay *et al.*, 2011; Naik & Jay, 2011; Templeton & Jay, 2013). Within this context, the LCR (1970-2004) mean annual fluvial-discharge, Q_{Wavg} , at the Beaver (Port Westward) gauge station (upstream boundary of study reach) is $\sim 6,780\text{m}^3\text{s}^{-1}$ (Fig. 3A; Naik & Jay, 2011). High-river stage winter and spring freshet daily peak-flows, Q_{Wpeak} , are typically moderated by dam release to between $15,000\text{-}17,000\text{m}^3\text{s}^{-1}$ (Fig. 3A; Gelfenbaum, 1983; Naik & Jay, 2011; Simenstad *et al.*, 2011), but may exceed bankfull conditions ($18,000\text{-}24,000\text{m}^3\text{s}^{-1}$) during extreme spring freshets (Sherwood *et al.*, 1990; Jay & Naik, 2011; Naik & Jay, 2011;). The inferred channel-bed slope, S_c , of the LCR is equal to $\sim 1.15 \times 10^{-5}$ (Hickson, 1912) as determined from the Columbia River Datum (CRD) low-tide and low-river stage water surface

slope (Fig. 3B). Over this gradient, the LCR experiences meso-tidal mixed diurnal and semidiurnal tides where the mean diurnal tidal prism is $11.0 \times 10^8 \text{ m}^3$ (Walton & Adams, 1976), and the mean range of tide (MN) and highest astronomical tide are 1.7 and 3.6m respectively at its mouth, and 2.0 and 4.0m near Astoria, OR, as the result of marginal tidal-funnelling (Fig. 3B; Fain *et al.*, 2001; Simenstad *et al.*, 2011). At low-river stage, the LCR maximum tidal-limit extends to ~ rkm 235 (Fig. 3B; Bonneville Dam), but tidal-modulation of the water surface height decreases to < 0.2m at Vancouver, WA (rkm 172; Kukulka & Jay, 2003), whilst observable current reversals extend to ~ rkm 109 (Fig. 3B; Clark & Snyder, 1969). These tidal-characteristics are similar to other less human-influenced fluvio-tidal systems along the central Cascadia Margin, USA, whose tides originate from the same amphidromic point (Table 1).

The hydrographic ratio, H_g , which equals $(Q_{tide}/Q_{Wavg}) \times 6hrs$ (1/2 a tidal cycle), where Q_{tide} is the mean diurnal tidal prism, is a commonly used parameter (cf. Peterson *et al.*, 1984) to compare the large-scale balance between tidal and fluvial energy input between differing fluvial-tidal systems, where an $H_g > 10$ suggests tidal-dominance, and systems with an $H_g < 10$ are considered fluvially-dominated. With respect to the LCR, its H_g is equal to 7, and it is therefore fluvially dominant (Table 1). Further evidence for LCR fluvial dominance throughout the study reach comes from: i) hydraulic surveys of Jay (1984) that were conducted over multiple tidal-cycles and low- to high- river stages (Fig. 4A), and ii) LCR numerical modelling results (cf. Hamilton, 1990; Sandbach *et al.*, 2018). By computing the dissipation of potential tidal- vs fluvial- energy across modern LCR channel cross-sections (cf. Jay, 1984), Jay *et al.* (1990) divided the FTT (~ rkm 0-235) into three hydraulic reaches (Figs 3B and 4A). 1) The most downstream reach is the tidally-dominated regime (TDR) spanning ~ rkm 0-21 that, during both low- and high- river flows, is characterized by strong bidirectional tidal-currents,

saltwater intrusion, development of a TM, and oceanic-derived waves at its seaward end (cf. Fox *et al.*, 1984; Sherwood & Creager, 1990; Figs 3B and 4A). 2) The mixed tidal-fluvial regime (MTFR) extends from ~ rkm 21-56, where fluvial-currents are dominant as the result of moderate- to high- river stages (Fig. 4A). At low-river stage, however, tidal-currents become more effective, and salinity intrusion may extend to ~ rkm 50 (Fox *et al.*, 1984; Chawla *et al.*, 2008; Figs 2A and 3B). Furthermore, within the MTFR, fluvial- and tidal- currents combine with intrabasinal wind-waves when atmospheric conditions are favourable (Fig. 4B). These short period (2.0-3.3s) wind-waves possess maximum heights of 0.2-0.7m with estimated near-bottom orbital velocities $> 0.2\text{ms}^{-1}$, which can re-suspend up to medium sands between ~ 1-4m in depth (Peterson *et al.*, 2014). The largest wind-waves are produced by west-southwest to east-northeast oriented winds from October to April, which occur during low-river flows (Figs 3A and 4B). Conversely, smaller wind-waves are produced by north-northwest to south-southeast oriented winds from May to September that tend to develop during higher-river flows (Figs 3A and 4B). 3) The fluvially-dominated, tidally-influenced regime (FDTIR) spans ~ rkm 56-235 (Fig. 3B), and at all river-stages is governed by downstream-oriented currents (Fig. 4A). At low river-stage, however, flood-tides cause fluvial-currents to experience: i) weak reversals to ~ rkm 109 (Clark & Snyder, 1969; Fig. 3B), and ii) cyclic velocity reduction and acceleration upstream of ~ rkm 109. In summary, integration of all hydraulic processes operating over the LCR study reach produces a temporally averaged 'global' conceptual relative energy diagram (Fig. 5A), which shows that: i) downstream-oriented currents are the 1st order control on sediment transport within the MTFR, whilst upstream-oriented flood tidal-currents and intrabasinal wind-wave oscillatory-currents are 2nd order controls, and ii) downstream-oriented currents dominate sediment transport within the FDTIR.

(B) Modern LCR sediment supply

The LCR mean annual sediment-load, Q_s , where $Q_s = Q_{sand} + Q_{wash}$ (where Q_{sand} represents bedload + suspended-load particles > 0.1 to ≤ 2 mm, and Q_{wash} represents suspended-load particles ≤ 0.1 mm), is derived from upstream drainage basin sources and tributaries (above \sim rkm 172), and is conveyed downvalley by large river-flows (Jay *et al.*, 1990; Sherwood *et al.*, 1990; Naik & Jay, 2011), whilst very little of its modern Q_s is sourced from the continental shelf (Gelfenbaum *et al.*, 1999; Templeton & Jay, 2013). The concentration of suspended fine sediment (≤ 0.062 to 0.1 mm; Q_{wash}) in the LCR is strongly a function of river-stage, where peak concentrations occur during high river-flows (Haushild *et al.*, 1966; Naik & Jay, 2011; Templeton & Jay, 2013), which is also supported by LCR high-flow plume research at its mouth and along the shelf (cf. Horner-Devine *et al.*, 2009). This same relation also holds for the TM of the LCR, which displays highest suspended-sediment concentrations (SSCs) during high-river stages that diminish during low-river stages (Gelfenbaum, 1983). Moreover, Gelfenbaum (1983) estimated that the maximum thickness of TM produced slackwater neap- and spring- tide fine sediment layers during low-river stage would be \sim millimetre-scale, and thus less than millimetre-scale upstream of the TM where SSCs are typically lower. From \sim rkm 0-40, LCR thalweg sediment, Q_{sand} , ranges from fine to medium sand (0.2-0.5mm), and coarsens marginally to medium to coarse sand (0.25-0.75mm) from \sim rkm 40-235 (Fox *et al.*, 1984; Sherwood & Creager, 1990; Fig. 3B). Due to the sand-rich nature of the LCR, the most important component of Q_s is its Q_{sand} fraction (Templeton & Jay, 2013). However, many researchers have concluded that the Q_s of the modern LCR, and especially its Q_{sand} (after 1940), have been significantly reduced by post-dam sediment trapping, and reductions in Q_{Wavg} due to

land irrigation, dam regulated discharge, and climate change (Sherwood *et al.*, 1990; Gelfenbaum *et al.*, 1999; Naik & Jay, 2005; Jay & Naik, 2011;; Naik & Jay, 2011; Templeton & Jay, 2013). Hindcast estimates below ~ rkm 172 suggest that pre-1900 Q_s was ~ 20 Mtyr⁻¹ ($Q_{sand} \approx 10$ Mtyr⁻¹; Gelfenbaum *et al.*, 1999; Naik & Jay, 2011), but has decreased to ~ 8 Mtyr⁻¹ ($Q_{sand} \approx 3.2$ Mtyr⁻¹) after 1970 within the post-dam era (Naik & Jay, 2011; Fig. 5B). In comparison, analyses of the lower Columbia River Valley (LCRV; ~ rkm 0-235) and continental-shelf sediment budget suggest that LCR longer-term Holocene averaged (last ~ 10,000 yrs) Q_s was 10-20 Mtyr⁻¹, where ~ 75% (7.5-15 Mtyr⁻¹) of this sediment was exported to the shelf, thus leaving a balance of 2.5-5 Mtyr⁻¹ to fill the LCRV to its current level (Fig. 5B; Gelfenbaum *et al.*, 1999; Baker *et al.*, 2010; Peterson *et al.*, 2013).

Furthermore, Templeton & Jay (2013) produced new hindcast predictions of the LCR Q_{sand} fraction from ~ 1900-2010, which include the Q_{sand} contributions of the Willamette and Cowlitz Rivers, to re-evaluate the balance of potential Q_{sand} supplied to the LCR below ~ rkm 109 against that removed via dredging and sand-mining . Their results suggest the LCR has experienced a net Q_{sand} deficit for > 50 of the last 85 years, and since 1962 this deficit has averaged ~ 4.6 (± 1.7) Mtyr⁻¹ (Templeton & Jay, 2013). The Q_{sand} results of Sherwood *et al.* (1990) and Templeton & Jay (2013) imply that since ~ 1940 the LCR should be reacting to declining Q_{sand} via ‘natural’ channel-bed and/or barform degradation below the Bonneville Dam (cf. Williams & Wolman, 1984; Schmidt & Graf, 1990; Topping *et al.*, 2000a,b; Rubin *et al.*, 2002; Grant *et al.*, 2003; Graf, 2006). However, no definitive ‘natural’ channel-bed or barform degradational observations exist, and instead: i) the main navigation channel from ~ rkm 5-172 has been artificially deepened by a total of ~ 2.4m since 1965, and ii) barforms, sand shoals, and floodplains, positioned between ~ rkm 0-80 in peripheral bays adjacent to the navigation channel

(i.e., Cathlamet Bay) have been aggrading for the last 100 to 1,000 yrs (Sherwood *et al.*, 1990; Peterson *et al.*, 2014; Prokocki *et al.*, 2015).

(B) Modern FTT barform migration rates

Time-sequenced aerial imagery from 1990-2011 (Bar BT1-P; FDTIR) and from 1990-2012 (Bars CB1-S and CB2-W; MTFR) was utilised to measure and compare the migration rates of bars positioned within secondary less human altered channels possessing closer to natural hydraulic properties (Sherwood *et al.*, 1990) relative to the adjacent heavily dredged main navigation channel (cf. Sherwood *et al.*, 1990; Jay, 2009; Jay *et al.*, 2011; Naik & Jay, 2011; Templeton & Jay, 2013), and within differing LCR fluvial-tidal hydraulic regimes (Fig. 6A-C). By tracking the centre of each bar from 1990 to 2011, or 2012, it is shown that Bar BT1-P migrated at an average rate of $\sim 7\text{myr}^{-1}$, whereas Bars CB1-S and CB2-W possessed near equal average migration rates of $\sim 24\text{myr}^{-1}$ (Fig. 6A-C). Migration patterns thus indicate that Bar BT1-P underwent primarily lateral-migration with minimal downstream translation in conjunction with vertical aggradation, whilst Bars CB1-S and CB2-W were governed by downstream translation and marginal lateral-migration (Fig. 6A-C). The differences in the rates and patterns of bar migration between Bar BT1-P (FDTIR) and Bars CB1-S and CB2-W (MTFR) are due to 'local' hydraulic effects, and not 'global' hydraulic effects. For instance, from a 'global' energy perspective (Fig. 4A), Bar BT1-P (FDTIR) should experience stronger, and more frequent, downstream-oriented currents than Bars CB1-S and CB2-W (MTFR). Thus, the 'global' expectation is that Bar BT1-P should display faster downstream migration rates than Bars CB1-S and CB2-W, but instead the opposite is true. This is because 'locally' Bar BT1-P formed in a

secondary channel arm of the LCR that is cut-off from LCR discharge, which is mainly confined to the adjacent main navigation channel (Fig. 6A). Conversely, Bars CB1-S and CB2-W formed within Prairie/Woody Island Channel network, Cathlamet Bay (i.e., secondary channel arm to adjacent main navigation channel; Fig. 6B and C), which ‘locally’ still receives a significant portion of LCR discharge and downstream-oriented current energy (cf. Sandbach *et al.* 2018). Therefore, even though Bars CB1-S and CB2-W exist in a lower ‘global’ downstream-oriented current regime when compared to Bar BT1-P (Fig. 4A), the ‘local’ frequency and magnitude of downstream-oriented current energy remains greater in the Prairie/Woody Island Channel network (MTFR) vs the south arm secondary channel of the FDTIR where Bar BT1-P formed.

Herein, the sedimentological details and interpretations of these three migrating FTT mid-channel bars of the LCR are presented. The first barform investigated (Bar BT1-P; rkm 80; FDTIR) formed within freshwater upstream of both the zone of TM development and salinity intrusion (Fig. 2A), where ~ 3.5km of GPR data (13 transects) and 3 vibracores were collected (Fig. 2B). Next, two barforms (Bar CB1-S and CB2-W) were analysed within the upper-MTFR, which are located upstream of the zone of TM development, but near the maximum extent of present low-river stage salinity intrusion, within Prairie Channel, Cathlamet Bay (Fig. 2C and D). At Bar CB1-S (~ rkm 42), ~ 3.9km of GPR data (12 surveys) and 3 vibracores were extracted, whereas ~ 3.8km of GPR data (17 surveys) and 3 vibracores were collected at Bar CB2-W (Fig. 2A). This data represents the first high-resolution geophysical and sediment core observations of modern FTT barforms that formed within a multi-channelled sand-bed, large-river ($Q_{Wavg} \sim 7,000\text{m}^3\text{s}^{-1}$, and $Q_{Wpeak} \geq 15,000\text{m}^3\text{s}^{-1}$), and that were potentially influenced by river-currents, and/or long period (tidal) and short period (wind-wave) oscillatory-currents.

(A) METHODS OF ANALYSIS

(B) GPR surveying and post-processing

Common-offset GPR transects (42 in total; ~ 11.2km) were collected via a Sensors & Software pulse-EKKO 100 smartcart system upstream of the region of saltwater saturation. Radar velocity through the freshwater-saturated sediment was determined from common mid-point surveys (CMPs) using normal move-out corrections. Two-way travel time was then converted to depth using a constant velocity of 0.054 m ns^{-1} (± 0.004), where the maximum depth of imaging was ~ 10m. Post-processing of survey-lines was completed in Seismic Unix software, which included: i) the application of a zero-phase, sine-tapered bandpass filter with polygon frequency values of 10, 50, 250, and 600 MHz, ii) time-based gaining of the data to reduce loss of reflection amplitude with depth, and iii) Stolt-migration based on a single subsurface velocity to reduce refraction hyperbolae. All GPR-profiles were then interpreted by classifying the most prominently repeating reflector geometries into distinct radar facies (see Best *et al.*, 2003; Sambrook Smith *et al.*, 2006, 2009; Mumpy *et al.*, 2007; Ashworth *et al.*, 2011; Parker *et al.*, 2013; Reesink *et al.*, 2014). Following the approach of Sambrook Smith *et al.* (2006, 2009), the areal occurrence (%) of each radar facies was computed for all GPR-profiles collected to examine the spatial distribution of facies within each bar. Next, the vertical occurrence (%) of facies within each bar was analysed by dividing each GPR-profile into regular intervals (1m thick), as measured upwards from the barform base. The proportion of facies within each vertical interval was then determined and summed, thus enabling the quantification of vertical facies distributions.

(B) Vibracore collection and analysis

Vibracores ($\leq 5\text{m}$ depth) were extracted using a $\sim 0.076\text{m}$ diameter aluminium irrigation pipe vibrated to depth by a portable vibracore rig. At each of the three barforms investigated (Fig. 2A-D), a single vibracore was taken from the head, mid-bar, and bartail, to capture potential sedimentological variation parallel to flow-direction (total of three cores per bar). After extraction, all cores were cut in half lengthways, where one half was set in epoxy resin to preserve sedimentary structures, whilst the other half was used for grain size sampling. Grain size samples were collected every $\sim 0.2\text{m}$ from the base of each core to its top, and in unique horizons such as silt drapes and coarse-grained interbeds. All samples were analysed via laser-diffraction size analysis (LDSA) using a Malvern Mastersizer 2000 (Malvern Instruments Limited, Malvern, UK) to acquire: i) their relative percentage of clay ($< 0.0039\text{ mm}$), silt (> 0.0039 to $< 0.063\text{ mm}$), and sand (> 0.063 to $< 2\text{ mm}$) particles, and ii) grain size distributions. Additionally, the Folk & Ward (1957) sorting index was computed for each sample. The D_{50} grain size and sediment sorting results of individual cores were then plotted against descriptive sedimentary logs to identify fining- and coarsening- upwards and sediment sorting trends in relation to the preserved depositional fabrics. These core results were then applied to the corresponding GPR-profiles in order to ground-truth the sedimentological interpretation of radar facies.

(A) RESULTS

(B) Sedimentology of radar facies

The general descriptions, spatial-scales, and examples, of the four radar facies identified in GPR-transects are presented in Table 2. However, the following will only explore the detailed

sedimentological observations and variations for the three primary radar facies (facies 1-3; Table 2) preserved within individual, and between FTT barforms, via specific GPR-profile examples and associated vibracore sedimentary logs. Radar facies 4 is excluded from analysis beyond that provided in Table 2, because no sedimentological evidence was observed in the vibracores obtained, and its representation within barforms is insignificant ($\leq 0.01\%$ in occurrence) relative to facies 1-3. Lastly, Table 3 presents the key to sedimentary logs, and defines pertinent tidal- and wind- elevation markers displayed on GPR-profiles and core logs.

(C) Radar facies 1a (Bar BT1-P; FDTIR): description and interpretation

Facies 1a consists of stacked, continuous, low-angle ($< 5^\circ$) parallel reflectors composed of clean cross-laminated moderately- to well- sorted fine to medium sands with interbeds of thin ($< 0.05\text{m}$ thick) concentrated horizons of organic detritus, sporadic inclusions of organic debris, and a homogenous $\sim 0.4\text{m}$ thick interbed of silt-rich very poorly-sorted very-fine sand bounded above and below by clean moderately-well to well-sorted fine to medium sands (Fig. 7A).

Interpretation: In the FDTIR, facies 1a represents low-angle dipping ($< 5^\circ$) upper-subtidal to intertidal bartail deposits (profile BT1-PY3, Fig. 8) formed by the aggradation of current-ripples to small-dunes that can be interbedded with up to $\sim 0.4\text{m}$ thick cross-laminated silty very-fine sand horizons. Fine-grained interbeds form via suspended-sediment fallout, and subsequent reworking, into current-ripples within the low-velocity bartail recirculation-cell produced by flow-separation around bars during a single, or multiple, high-river stage event(s) (cf. Leeder & Bridges, 1975; Nanson & Page, 1983; Smith *et al.*, 2009, 2011; Moreton & Carter, 2015).

(C) Radar facies 1b (Bar CB1-S; upper-MTFR): description and interpretation

Facies 1b is imaged as stacked, continuous, low-angle ($< 5^\circ$) parallel reflectors, and consists of clean cross-laminated moderately-well to well-sorted fine to medium sands with sporadic to abundant ($< 0.08\text{m}$ thick) planar-laminated macroscopic organic horizons with, or without, pumice gravel. Facies 1b fines-upward from its base (i.e., becomes dirtier) before coarsening-upward and becoming better sorted towards its top (Fig. 9A-C). However, facies 1b does vary across Bar CB1-S (barhead to bartail) with respect to the frequency, thickness, and fabric, of silt to very-fine sand intervals, which can be (Fig. 9A-C): i) a $\sim 1\text{m}$ thick heterogeneous bed with interbedded $< 0.08\text{m}$ thick organic layers and $< 0.1\text{m}$ thick horizons of cross-laminated fine sands (barhead), ii) infrequent thin ($\leq 0.05\text{m}$ thick) silt drapes (mid-bar), or iii) completely absent (bartail). Facies 1b typically overlies facies 2 or 3, but may interbed with facies 3 near bar-tops ($\sim 0\text{-}3\text{m}$ depth; Fig. 10). **Interpretation:** Facies 1b is interpreted as the reworking of bartop upper-subtidal to intertidal 3D trough cross-stratified to high-angle ($> 5^\circ$) cross-bedded dune to unit-bar scale deposits, generated by the combined-influence of intrabasinal wind-waves and tidally-produced cyclic shallow water flooding- and drainage- currents (cf. Prokocki *et al.*, 2015) that form low-angle dipping ($< 5^\circ$) longitudinal- and lateral- bar accretion packages (Fig. 10). Similar low-angle accretion-units in subaqueous sandbanks of the Marennes-Oleron Bay, France, have been observed, and are likewise interpreted to be the product of oceanic wave-tidal combined-flows (see figures 9-11 of Chaumillion *et al.*, 2008). Furthermore, when facies 1b displays abundant silt/very-fine sand drapes ($< 0.05\text{m}$ thick), or silty-sand horizons (0.1 to $> 0.4\text{m}$ thick), this represents: i) high-river discharge Q_{wash} sediment-fallout within recirculation-cells produced by flow-separation around Bar CB1-S, or flow deceleration of downstream-oriented currents caused by flow divergence at swatchway entrances (i.e., barhead of Bar CB1-S), , and/or ii) low-river stage re-entrainment, and redistribution, of high river-stage and/or

slackwater deposited Q_{wash} (potentially from bartail towards barhead) via intrabasinal wind-waves working in conjunction with flood-tidal currents.

(C) Radar facies 1c (Bar CB2-W; upper-MTFR): description and interpretation

Facies 1c is also depicted as stacked, continuous, low-angle ($< 5^\circ$) parallel reflectors, but unlike facies 1a and 1b, it exists typically from bartail to barhead as bioturbated fine to medium sands with sporadically preserved plant debris or pumice gravel with (Fig. 11A-C): i) intensely bioturbated, or churned, horizons (> 0.1 to < 1.5 m thick) of silt to fine-sand (Fig. 11B and C), or ii) abundant silt drapes that are < 0.05 m thick. However, low-angle planar- to cross- laminated sets are present in horizons with minimal bioturbation. Similar to facies 1b, facies 1c tends to fine-upwards from its base, and then coarsens and becomes better sorted upward near its top (Fig. 11B and C), but only displays a coarsening- and sorting- upwards trend from its base to top in bartail alluvium (Fig. 11A). Facies 1c typically overlies facies 2 or 3, and like facies 1b tends to be interbedded with facies 3 near bar-tops (~ 0 -3m depth; Line CB2-WX6; Fig. 12).

Interpretation: Similar to facies 1b, facies 1c also represents the reworking of bartop upper-subtidal to intertidal 3D trough cross-stratified to high-angle ($> 5^\circ$) cross-bedded dune to unit-bar scale deposits into low-angle dipping ($< 5^\circ$) longitudinal- and lateral- bar accretion packages (Fig. 12). The abundant silt to very-fine sand drapes and intervals are interpreted as Q_{wash} sediment-fallout within recirculation-cells produced by flow-separation around Bar CB2-W during high-river discharge, and/or low-river stage redistribution of high-river stage and/or slackwater produced silts to very-fine sands via intrabasinal wind-waves in association with tidal-currents. However, since facies 1c is much dirtier and bioturbated relative to facies 1b, it is

thought that the rates, and strength, of wind-wave reworking of alluvium are weaker during the creation of facies 1c.

(C) Radar facies 2a: (Bar BT1-P; FDTIR): description and interpretation

Facies 2a is imaged as high-angle ($> 6^\circ < 20^\circ$) inclined reflectors composed of planar- to cross-laminated bedded moderately-well to well-sorted fine to medium sands with sporadic organic debris, a few thin (< 0.08 m thick) interbeds of concentrated organic detritus, and several < 0.05 m thick silty very-fine sand drapes (Fig. 7B). This facies also shows a marginal fining-upwards trend from well-sorted basal medium sands to dirtier, moderately well-sorted, fine sands, whose silt rich intervals are poorly-sorted (Fig. 7B). ***Interpretation:*** Facies 2a represents high-angle dipping subtidal to intertidal bar-margin lateral-accretion sets (Line BT1-PX5; Fig 8), where fine-grained interbeds are the product of non-cyclic, or sporadic, suspension fall-out of Q_{wash} during high-fluvial discharge intervals within low-velocity sidebar recirculation-cells that are created as seaward-directed main flow detaches around barheads.

(C) Radar facies 2b: (Bar CB2-W; MTFR): description and interpretation

Facies 2b consists of high-angle inclined reflectors composed of silt-rich moderately to very-poorly sorted very-fine to fine sands that are intensely bioturbated, but cross-laminae sets are present where bioturbation is less intense (Fig. 11A). ***Interpretation:*** This facies is interpreted as subtidal avalanche faces of prograding bartail accretion-sets (Fig. 12), where silt drapes to bioturbated silty-sand horizons are the product of: i) non-cyclic capture of high-river stage Q_{wash} within low-velocity bartail recirculation-cells, ii) more cyclic deposition of high-river stage Q_{wash} during flood-tides, and tidal slackwater, when the velocity of downstream-oriented

currents is reduced, iii) low-river stage re-entrainment of Q_{wash} via wind-waves and tidal-currents that is more cyclically redeposited during tidal slackwaters, and/or redeposited as suspended-sediment fallout when wave-energy diminishes, or iv) a combination of i), ii) and iii).

(C) Radar facies 3 (FDTIR and MTFR): description and interpretation

Throughout all FTT regimes, facies 3 consists of stacked-sets of laterally-discontinuous undular (concave-up or concave-down) to chaotic reflectors, which are composed of clean moderately-well to well-sorted cross-bedded medium sands with sporadic interbeds (< 0.08m thick) of concentrated organic debris and gravel-sized pumice stones (Fig. 7A-C). Facies 3 occurs as barhead to bartail alluvium that fines-upward from base to top, but may possess second-order decimetre-scale fining- and coarsening- upward sequences (Fig. 7A). Within the FDTIR, facies 3 is deposited at subtidal to intertidal elevations (Fig. 8), whilst it is more commonly preserved at subtidal depths within the MTFR (Figs 10 and 12). ***Interpretation:*** Facies 3 represents vertically-stacked 3D dune to unit-bar trough-cross and cross-bedded deposits within longitudinal- and lateral- accretion packages, which are commonly found in river braid-bars (cf. Bridge, 1993; Bridge *et al.*, 1998; Bridge, 2006). The largest trough-shaped reflectors are found at greater depths (~ 6-10m), whilst progressively becoming smaller-scale towards bartops (Fig. 8). This vertical gradient in reflectors corresponds to a decrease in flow depth towards bartops, which forces a reduction in the height and wavelength of dunes and unit-bars (Yalin, 1964; Allen, 1978). Parallel reflectors in this facies are thus bounding surfaces between either (Fig. 8): i) dune-scale cross-sets, ii) unit-bar accretion-sets, or iii) bar-scale accretion-sets.

(B) Patterns of bar migration and occurrence of radar facies

(C) Bar BT1-P: FDTIR

From 1990-2011, Bar BT1-P underwent primarily vertical aggradation, but also experienced relatively slow ($\sim 7\text{myr}^{-1}$; Fig. 6A) southward-directed lateral-accretion, and marginal elongation via bartail-extension and barhead-accretion (see Supplemental Information). Within this context, the architecture of Bar BT1-P is dominated by facies 3 ($\geq 70\%$ areal occurrence in all GPR-transects; Fig. 13A). In the vertical, the occurrence of facies 3 is $> 80\%$ from its base to bar-top (10-0m depth; Fig. 13B), but can be $> 95\%$. However, facies 1a and 2a do exist in relatively low-occurrences between 0-6m depth ($\leq 11\%$; Fig. 13B), but are restricted to southern bar-margin lateral-accretion and bartail-extension (see lateral-lines PX4-PX9, and longitudinal-lines PY1, PY3, and PY4; Fig. 13A).

(C) Bar CB1-S: MTFR

Between 1990 and 2012, this bar experienced relatively high-rates of downstream-translation ($\sim 24\text{myr}^{-1}$; Fig. 6B) that transformed its morphology from elongated to more arcuate, which promoted development of bartail-limbs (see Supplemental Information). Relative to Bar BT1-P, Bar CB1-S possesses a different morphology (arcuate *vs* elongated), and developed within a differing hydraulic context punctuated by dominant seaward-oriented currents, stronger upstream-oriented flood-tidal currents, and intrabasinal wind-waves. Given these differences, the resulting architecture of Bar CB1-S varies from that of Bar BT1-P in several ways. First, in Bar CB1-S profiles, the overall occurrence of facies 3 reduces by $\sim 30\text{-}60\%$ to $\leq 45\%$ within longitudinal-transects (SY1-SY4), and reduces by $\sim 10\text{-}60\%$ to $\leq 60\%$ in lateral-profiles (SX1-SX8; compare Figs 13A and 14A). Secondly, facies 1 transforms into facies 1b, and increases in occurrence by $\sim 40\text{-}85\%$ to $\geq 55\%$ in longitudinal-profiles, whilst increasing to between 10-85%

in lateral-lines (Fig. 14A). Thirdly, at Bar CB1-S, facies 1b displays a continual increase in occurrence from its base to bartop, where it is $\leq 7\%$ from 5-7m depth, whilst drastically increasing to $\sim 34\text{-}55\%$ from 3-5m depth, which is within the projected depth window of intrabasinal wind-wave influence at MLLW (MaxW2; Fig. 14B). Facies 1b then further increases in abundance to $\sim 80\text{-}90\%$ within the depth window of intrabasinal wind-wave activity at MHHW (MaxW1; 0-3m depth) near its top (Fig. 14B). Simultaneously, from its base to bartop, facies 3 decreases in occurrence from $\sim 60\text{-}96\%$ from 4-7m depth to $< 30\%$ from 0-4m depth through MaxW2 and MaxW1 (Fig. 14B). Furthermore, facies 2a also exists in relatively low-occurrence ($< 2\%$) from 4-7m depth before notably increasing to $\sim 13\text{-}17\%$ near its bartop ($\sim 2\text{-}4\text{m}$ depth; Fig. 14B). These facies trends do not exist at Bar BT1-P, which is dominated from base to bartop by the vertical-stacking of facies 3.

(C) Bar CB2-W: MTR

From 1990 to 2012, Bar CB2-W (positioned $\sim 2\text{km}$ southwest of Bar CB1-S within Prairie/Woody Island Channel) underwent (Fig. 6C, and Supplemental Information): i) downstream translation equal to $\sim 24\text{myr}^{-1}$, ii) volumetric growth in the form of lateral-expansion, and iii) development of bartail-limbs. Since Bars CB1-S and CB2-W are located within the same channel and FTT regime, share a similar arcuate morphology, and experienced analogous migration rates and patterns, the expectation is that they will possess nearly identical facies occurrences and stacking patterns. In general, the architecture of these two bars are more closely related to one another than Bar BT1-P, but there are several notable differences. First, at Bar CB2-W, facies 1 transforms into facies 1c and facies 2 becomes facies 2b. However, in general, the longitudinal-profiles of Bar CB2-W also mainly comprise facies 1 ($\geq 45\%$; form of

facies 1c) and facies 3 (0-55%; Fig. 15A), but they possess a ~ 2-15% higher occurrence of facies 2 (form of faces 2b) relative to facies 2a at Bar CB1-S (see Figs 14A and 15A).

Furthermore, the barhead to bartail lateral-lines (WX1-WX11) of Bar CB2-W have a higher (~ 40% on average) abundance of facies 3, and an average lower occurrence (~ 25%) of facies 1 in the form of facies 1c.

Furthermore, in the vertical direction at Bar CB2-W, facies 1c continually increases in occurrence from its base to bartop, as also observed in facies 1b at Bar CB1-S, but the pattern of this increase differs. Within Bar CB2-W, the occurrence of facies 1c spans ~ 6-18% between 3-6m depth (base of MaxW2), which then increases rapidly at the base of MaxW1 to ~ 45% at 2-3m depth, and then continues to increase towards the top of MaxW1 from ~ 60% (1-2m depth) to ~ 70% between 0-1m depth (Fig. 15B). Comparatively, at Bar CB1-S, facies 1b has a much higher occurrence (≥ 30 -82%) throughout the 3-5m depth interval (i.e., within MaxW2), and does not decline below ~ 10% until below MaxW2 at 5-6m depth (Fig. 14B). Secondly, and resembling the trend at Bar CB1-S, the occurrence of facies 3 here also decreases from base to bartop, but not to the same degree. At Bar CB2-W, the occurrence of facies 3 is ≥ 70 % between 3-7m depth (i.e., from within MaxW2 to below MaxW2) before reducing through MaxW1 to ~ 45% (2-3m depth), and then to ~ 25% from 0-2m depth (Fig. 15B). Relative to Bar CB1-S, however, the average preservation of facies 3 is much greater (~ +25%) from 0-5m depth through the MaxW2 and MaxW1 wind-wave windows. The final divergence in facies occurrence with depth between Bars CB1-S and CB2-W appears within the depth interval spanning 0-2m, where at Bar CB2-W the proportion of facies 2b ranges from ~ 8-15%, whilst at Bar CB1-S any style of facies 2 is absent (see Figs 14B and 15B).

(A) DISCUSSION

(B) Linking FTT hydraulics to barform architecture and IHS

(C) Large-river FDTIR mid-channel bars

Although Bar BT1-P (FDTIR) experiences cyclic bidirectional-currents and slackwater intervals, its architecture is nearly identical to that of linear, or elongated, fluvial braid-bars experiencing more vertical-aggradation relative to lateral- and/or longitudinal- accretion (cf. Sambrook Smith *et al.*, 2006, 2009; Mumpy *et al.*, 2007; Ashworth *et al.*, 2011; Parker *et al.*, 2013; Reesink *et al.*, 2014). Thus, downstream-oriented currents, especially river-flood events (Dalrymple *et al.*, 2015), govern the bed- to bar- scale sedimentology of LCR braid-bars throughout its FDTIR, whilst flood-tidal currents, and slackwater periods (four daily), seem to exert little influence. This finding is supported by i) fluvial dominance throughout the FDTIR of the LCR (Fig. 4A), and ii) the numerical simulations of van de Lageweg & Feldman (2018) who found that the landward-most braid-bars within micro- to meso- tidal range FTTs tend to have a sedimentological architecture dominated by seaward-oriented currents. Therefore, with respect to longer-term preservation, this suggests that ~ 76% (~ rkm 56-235; FDTIR) of the LCR basal to bar-top braid-bar successions within its FTT will be indistinguishable from upstream fully-fluvial braid-bars.

Furthermore, this finding also suggests that FDTIR braid-bar bartail and bar-margin accretion-sets with sporadic silty very-fine sand horizons (> 0.2m thick), and thin (< 0.05m thick) silty very-fine sand drapes, are unlikely to be tidally-produced IHS packages as commonly interpreted (cf. Smith, 1987; Sisulak & Dashtgard, 2012; Johnson & Dashtgard, 2014; Dalrymple *et al.*, 2015). Instead, they represent fluvially derived decimetre-scale low-angle (< 5°) non-cyclic IHS of bartail accretion-sets, and high-angle (> 5° ≤ 20°) sub-decimetre scale bar-

margin non-cyclic IHS within lateral-accretion units (Fig. 16A). These IHS packages are likely deposited during high-river stage(s) within low-velocity bartail and side-bar flow recirculation-cells when LCR river-derived Q_{wash} concentrations are highest (cf. Haushild et al. 1966; Naik & Jay, 2011; Templeton & Jay, 2013). Furthermore, these are the same hydraulic-sedimentation processes that produce fluvial IHS in bartail- and lateral- accretion sets of modern sand-bed, large-river braid-bars (Bristow, 1993; Best *et al.*, 2003; Reesink *et al.*, 2014), modern and ancient counter point-bar accretion-sets (Smith *et al.*, 2009, 2011; Durkin *et al.*, 2015), and downstream-most point-bar lateral-accretion successions (Thomas *et al.*, 1987; Hubbard *et al.*, 2011; Durkin *et al.*, 2015; Moreton & Carter, 2015).

(C) Large-river MTFR mid-channel bars

Bars CB1-S and CB2-W display relatively high rates of downstream-translation, arcuate morphologies, and associated bartail-limb construction, which are typical attributes of migrating fluvial and/or fluvial-tidal braid-bars (cf. Ashworth, 1996; Best *et al.*, 2003; Reesink *et al.*, 2014; Leuven *et al.*, 2016). Thus, similar to FDTIR braid-bars of the LCR, these patterns of morphology and migration suggest that seaward-directed currents, especially high-river flows, govern their bed- to bar- scale sedimentology, which is not surprising since the mesotidal LCR is fluvially, or ebb-tidal, dominant. Given this context, the stratal architectures of Bars CB1-S and CB2-W should be similar to one another, as well as FDTIR braid-bars, and should also be comparable to other sand-bed, large-river braid-bars undergoing downstream-translation (i.e., Río Paraná, Argentina; see Sambrook Smith *et al.*, 2009; Reesink *et al.*, 2014). However, Bars CB1-S and CB2-W do not possess a similar architecture to FDTIR bars, nor are they identical to

one another (see Figs 13, 14, and 15), and their architecture is incongruous with translating Río Paraná bars.

For instance, bars of the Río Paraná tend to have stratal architectures dominated by relatively clean longitudinal- and lateral- accretion packages composed of (Sambrook Smith *et al.*, 2009; Reesink *et al.*, 2014): i) mid-bar to bar-top high-angle ($> 20^\circ$ to angle-of-repose) to medium-angle ($> 6^\circ < 20^\circ$) cross-strata associated with the migration of small to large-dunes, unit-bars, or bar-margin accretion (analogous to facies 2a of this study), and ii) basal vertically-stacked large- to small- scale trough-cross strata associated with migrating 3D dunes to unit-bars (analogous to facies 3 of this study). Comparatively, the basal strata of Bars CB1-S and CB2-W are similar to the Río Paraná and FDTIR bars of the LCR, except their bar-tops ($\sim 0\text{-}4\text{m}$ depth) display minimal preservation of high- to medium- angle cross-strata (facies 2a), and/or vertically-stacked trough-cross strata (facies 3), and instead consist of stacked-successions of low-angle ($< 5^\circ$) accretion, or facies 1b and 1c. Given that the stratal architecture of Bars CB1-S and CB2-W differ from one another, and are dissimilar to translating Río Paraná bars and FDTIR bars of the LCR, this implies that their overall sedimentology, especially bar-tops, is not solely the product of downstream-oriented currents, but must also reflect a secondary hydraulic-sedimentation response. At first glance, this finding supports the general view that mesotidal MTFR braid-bars of any FTT, regardless of fluvial-energy input (i.e., fluvial-discharge), should display a more complex bed- to bar- scale architecture in comparison to up-dip FDTIR and fluvial braid-bars due to increased bidirectional tidal-current energy (especially flood-tidal currents), and associated slackwater intervals (Dalrymple *et al.*, 2015; van de Lageweg & Feldman, 2018). However, the more complex bar-top architectural styles observed within MTFR Bars CB1-S and CB2-W are not simply the product of increased bidirectional tidal-

current energy, and associated slackwater intervals. Instead, these differences are interpreted herein to be the product of combined-flows consisting of a wind-wave oscillatory-current component and a bidirectional tidal-current component. One of the effects of this flow-field is reflected in the different locations, depositional fabrics, and styles, of bar-top IHS preserved within upper-MTFR bars (Fig. 16B, C).

Similar to Bar BT1-P (FDTIR), the majority of fine-grained sediment ($< 0.125\text{mm}$) preserved in the bar-top deposits of Bars CB1-S and CB2-W most likely originate from high-river stage events when Q_{wash} concentrations are highest, whilst very little comes from low-river stage slackwater intervals (cf. Gelfenbaum, 1983). Thus, IHS within these bars is expected to be concentrated within bartail and bar-margin accretion for the same reasoning applied to the IHS of Bar BT1-P. At Bar CB1-S, however, bartail-accretion is devoid of IHS, whilst low-angle ($< 5^\circ$) sub-decimetre scale cyclic IHS occurs in mid-bar accretion, and low-angle combined sub-decimetre to decimetre-scale cyclic IHS exists within barhead deposits (Fig. 16B). In comparison, bartail accretion at Bar CB2-W displays bioturbated sub-decimetre to decimetre-scale high-angle ($> 5^\circ$ to $\leq 20^\circ$) cyclic IHS that is bounded above by bioturbated sub-decimetre scale low-angle ($< 5^\circ$) cyclic IHS, whereas both mid-bar and barhead accretion-units possess bioturbated sub-decimetre scale low-angle cyclic IHS (Fig. 16C). Relative to large-river, fully-fluvial and FDTIR braid-bars, these MTFR bar-top variations in the character, depositional fabric, and/or locations of IHS, represent a new category of IHS. This style of IHS is interpreted to be the result of the re-entrainment, and redistribution, of fines deposited during high-river stage(s) by low-river stage combined-flows possessing varying magnitudes of a short period wind-wave oscillatory-current component and a long period bidirectional tidal-current component (with associated slackwater intervals) that will vary in strength over neap-spring tidal

cycles (Fig. 16B, C). This type of hydraulic-sedimentation response has not been documented before as a potential agent of IHS production within fluvial-tidal barforms (e.g., Smith, 1987; Thomas *et al.*, 1987; Sisulak & Dashtgard, 2012; Dalrymple *et al.*, 2015; Jablonski & Dalrymple, 2016).

Nevertheless, the effects of varying degrees of wind-wave oscillatory-current strength causes differing patterns of bar-top upper-MTFR IHS. Stronger and more frequent wind-wave activity causes the absence of IHS in bartail-accretion due to the re-suspension and removal of finer sediment from accretion-units that is then re-deposited in mid-bar and barhead recirculation-cells generated by flow-separation around bars during flood-tidal flows, and/or during slackwater intervals (Fig. 16B), or this re-suspended fine sediment is carried downstream away from the bartail by ebb-currents. Conversely, weaker, and less frequent, wind-wave activity allows for the development of bioturbated, and more abundant, IHS preserved within bartail to barhead accretion-sets, which experience overall lower rates of re-suspension, and thus redistribution of fines by tidal-currents (Fig. 16C). Lastly, when considering longer-term preservation across the FTT of the LCR, these findings suggest that ~ 82% (~ rkm 42-235; upper-MTFR to FDTIR) of basal braid-bar deposits are likely indistinguishable from up-dip fully-fluvial braid-bars, whilst, if preserved, upper-MTFR bar-top strata potentially mark the facies transition from fully-fluvial to wave-tidally dominated strata.

(C) Fluvial-tidal IHS preservation: mid-channel bars vs point-bars

The IHS preserved within the upper-MTFR to FDTIR bars of the LCR diverge from the IHS model for fluvial-tidal point-bars (Fig. 1) in several key ways. First, fluvial to fluvial-tidal point-bar IHS tends to have dip-angles $\geq 5^\circ$ to $\leq 35^\circ$ (more commonly $\sim 5-15^\circ$) that do not vary

spatially across a point-bar since their dip-angles are set by the transverse point-bar slope (Thomas *et al.*, 1987; Smith *et al.*, 2009; Durkin *et al.*, 2015; Moreton & Carter, 2015; Jablonski & Dalrymple, 2016). Furthermore, their fine-grained components of IHS are nearly always interpreted to reflect the hydraulic-sedimentation response of tidal processes (e.g., tidal slackwater, or turbidity-maximum enhanced deposition of fines) in conjunction with increased salinity-levels and brackish water ichnofacies (cf. Sisulak & Dashtgard, 2012; Johnson & Dashtgard, 2014; Dalrymple *et al.*, 2015). In contrast, LCR bar-top IHS of upper-MTFR to FDTIR braid-bars typically possess lower dip-angles ($< 5^\circ$) that are spatially more variable (can be $> 5^\circ$ to $\leq 20^\circ$; Fig. 16A-C), and formed in primarily freshwater conditions upstream of the turbidity-maximum, and typically lack bioturbation (with the exception of Bar CB2-W). Secondly, FDTIR bar-top IHS is produced solely by river hydraulic-sedimentation processes within a known tidally-influenced regime, whilst upper-MTFR bar-top IHS largely reflects varying degrees of intrabasinal wind-wave oscillatory-current strength, and/or frequency, with the secondary influence of tidal-currents, and associated slackwater intervals. Thirdly, any increase in the relative density and thickness of fine-grained interbeds within LCR bar-top IHS (i.e., overall increase in mud/silt to sand ratios of bars) from the FDTIR to upper-MTFR (as would be predicted by the fluvial-tidal point-bar model), depends upon the position of individual bars relative to the maximum intrabasinal wind-wave energy corridor. For example, bars located near the centre of the wind-wave energy corridor (Bar CB1-S) will be cleaner relative to much dirtier laterally-adjacent bars (Bar CB2-W) positioned closer to basin-bounding floodplain/tidal-flat environments that are laterally separated from the strongest, and most frequent, wind-wave energy pathway (cf. van de Lageweg *et al.*, 2018; Fig. 16B, C).

(C) *Does bar-top coarsening-upwards occur in fluvio-tidal mid-channel bars?*

A number of studies (Mutti *et al.*, 1985; Clark & Reinson, 1990; Shanmugam *et al.*, 2000; Feldman *et al.*, 2008; Feldman & Demko, 2015) have suggested that tidal-bars display an overall upward-coarsening sequence towards their tops. One possibility is that this is the result of differing coarse-grained sediment transport pathways during flood- and ebb- tidal flows on, and around, barforms (cf. Ghinassi *et al.*, 2018). However, the present data illustrate that the sedimentology of mid-bar to bar-top (~ 0-4m depth) alluvium of FDTIR braid-bars (Bar BT1-P) displays an overall fining-upwards sequence (Fig. 17A), whilst remaining moderately well- to well- sorted except in a few horizons of non-cyclic IHS. Thus, sandy FDTIR bars of the LCR contradict the upward-coarsening observations of interpreted tidal-bars (cf. Mutti *et al.*, 1985; Clark & Reinson, 1990; Shanmugam *et al.*, 2000; Feldman *et al.*, 2008; Feldman & Demko, 2015), and instead fine-upwards like fluvial braid-bars (cf. Ashworth *et al.*, 2011; Reesink *et al.*, 2014).

Conversely, within the MTFR, as tidal-current energy input increases and intrabasinal wind-waves become relevant, LCR bars exhibit coinciding coarsening- and sorting- upwards trends near their bar-tops (between ~1.5-0m depth; Fig. 17B, C). These bar-top coarsening- and sorting- upwards sequences are thought to represent the winnowing, or extraction, of finer sediment (< 0.25mm) at low river-stage from bar-top alluvium via the combined effects of tidally-produced bar flood- and ebb- currents and intrabasinal wind-waves (cf. Prokocki *et al.*, 2015; Fig. 18A, B). The winnowing of bar-top finer alluvium causes the preferential preservation of moderately well- to well- sorted coarser-grained bar-top sediments ($\geq 0.25\text{mm}$). The depth within the bar where the coarsening- and sorting- upwards sequence may appear (Fig. 17B, C), as well as the degree of bioturbation, depends upon the magnitude of wind-wave energy

a bar receives within a given period of time. Bars affected by maximum wind-wave energy, and thus the largest waves, will have their coarsening- and sorting- upwards bar-top sequence begin at greater bar depths, and will lack bioturbation, whilst when wind-wave energy is weaker, or less frequent, this sequence is initiated at shallower bar depths, but will have a higher probability of being bioturbated (Fig. 18A, B).

(A) CONCLUSIONS

The present study of mid-channel bars in the fluvial-tidal transition (FTT) of a large mesotidal river reveals four key findings:

- 1) As a consequence of high-river stage, the sedimentology of FTT bars is dominated by seaward-directed currents. This causes ~70% of FTT barforms to possess a base to bar-top sedimentary architecture that is indistinguishable from fluvial braid-bars, whilst $\geq 80\%$ of the basal (bar core) strata mimic that of fluvial braid-bars. This suggests that the FTTs of multi-channelled mesotidal large-rivers (mean annual discharge $\geq 7,000 \text{ m}^3\text{s}^{-1}$, and peak discharges $\geq 15,000 \text{ m}^3\text{s}^{-1}$) are likely dominated by mid-channel bar strata lacking clearly discerned tidal, or wind-wave, sedimentological markers.
- 2) Three styles of bar-top Inclined Heterolithic Stratification (IHS) characterize the FTT reach of the Lower Columbia River (LCR): 1) Fluvially-dominated, tidally-influenced regime, non-bioturbated low-angle ($< 5^\circ$) to higher-angle ($> 5^\circ$ to $\leq 20^\circ$) non-cyclic IHS, with fine-grained interbeds ($\leq 125\mu\text{m}$) that are deposited by high-river stage sedimentation processes within bartail and bar-margin accretion-sets, and are indistinguishable from fluvial braid-bar IHS ; 2) Upper-

mixed tidal-fluvial regime, non-bioturbated low-angle ($< 5^\circ$) cyclic IHS found in mid-bar to barhead accretion-packages; and 3) Bioturbated higher-angle ($> 5^\circ$ to $\leq 20^\circ$) cyclic IHS within avalanche faces of bartail accretion-units, and low-angle ($< 5^\circ$) cyclic IHS preserved mainly in mid-bar and barhead accretion-packages. The second and third styles represent a newly recognized form of IHS in FTT mid-channel barform strata produced by fine sediment that was deposited initially during high river-stage, but then is re-entrained and redistributed into bar accretion-sets by low river-stage combined-flows consisting of a wind-wave oscillatory-current and bidirectional tidal-currents. When the wind-wave oscillatory-current of this combined-flow is relatively weak, or less frequent, IHS within accretion-sets will be more abundant and bioturbated (i.e., style three).

3) When preserved, the second and third styles of upper-mixed tidal-fluvial regime freshwater IHS provide a distinct sedimentological signature within bar-top strata, which signifies the initial downstream crossover point in braid-bar architecture from up-dip fully-fluvial (from their bases to bar-tops), to down-dip facies that possess bar-top depositional fabrics produced by the hydraulic-sedimentation response of a combined wind wave-tidal influence.

4) The dip-angles of IHS within bar-top accretion-packages of LCR freshwater FTT mid-channel bars are typically $< 5^\circ$, but can be $> 5^\circ \leq 20^\circ$ when deposited within bartail extension-sets, and/or bar-margin lateral-accretion units. In contrast, bar-top dip-angles of fluvial, or fluvial-tidal, point-bar IHS typically range from $\sim 5-15^\circ$, and remain spatially constant throughout barhead to bartail accretion-sets. Bar-top IHS of FTT mid-channel bars is therefore more likely to display lower dip-angles on average that are spatially more variable within a given bar. Thus, when

evaluating the rock record, bar-top IHS with average dip-angles of $< 5^\circ$, which display greater spatial variability, thus provides a diagnostic feature to help determine if stratal sequences represent a single-threaded FTT with point-bars *or* a multi-channelled FTT with mid-channel bars.

Acknowledgements

This research was funded primarily by ExxonMobil, but was also supported by UK Natural Environment Research Council (NERC) grant awards NE/H007954/1, NE/H006524/1, NE/H007261/1 and NE/H00582X/1. We thank Mike Blum and Howard Feldman for their advice and insight during this research as well as the Clatsop Community College and Environmental Research and Training Station for providing space for field instrumentation, sediment core storage, and access to building equipment and tools. We also thank Kyungsik Choi and an anonymous reviewer for their insightful remarks that strengthened the final version of this manuscript. A special thank you goes to Michael Wilkin, Katie Rathmell and António Baptista, for their invaluable advice and expertise regarding the Lower Columbia River. We also extend thanks to Steve Sandbach, Kyle Balling, and Claire Keevil, for helping with data collection, and, lastly, we thank Pat Killion (captain of the Tansey Point) whose many years of navigational experience along the Lower Columbia River made this research possible.

REFERENCES

Allen, J.R.L. (1978) Computational methods for dune time-lag: calculations using Stein's rule for dune height. *J. Sed. Geol.*, **20(3)**, 165-216.

Ashworth, P.J. (1996) Mid-channel bar growth and its relationship to local flow strength and direction. *Earth Surf. Proc. Land.*, **21**, 103-123.

Ashworth, P.J., Sambrook Smith, G.H., Best, J.L., Bridge, J.S., Lane, S.N., Lunt, I.A., Reesink, A.J.H., Simpson, C.J. and Thomas, R.E. (2011) Evolution and sedimentology of a channel fill in the sandy braided South Saskatchewan River and its comparison to the deposits of an adjacent compound bar. *Sedimentology*, **58**, 1860-1883.

Baker, D., Peterson, C., Hemphill-Haley, E., and Twichell, D. (2010) Latest Pleistocene and Holocene (2-16 ka) sedimentation in the Columbia River estuary, Oregon, USA. *Mar. Geol.*, **273**, 83-95.

Berné, S., Vagner, P., Guichard, F., Lericolais, G., Liu, Z., Trentesaux, A., Yin, P., and Yi, H.I. (2002) Pleistocene forced regressions and tidal sand ridges in the East China Sea. *Mar. Geol.*, **30**, 293-315.

Best, J.L., Ashworth, P.J., Bristow, C.S. and Roden, J. (2003) Three-dimensional sedimentary architecture of a large, mid-channel sand braid bar, Jamuna River, Bangladesh. *J. Sed. Res.*, **73(4)**, 516-530.

Boyd, R., Dalrymple, R.W. and Zaitlin, B.A. (2006) Estuary and incised valley facies models. In: *Facies Models Revisited* (Eds H.W. Posamentier and R.G. Walker), *SEPM Spec. Publ.*, **84**, 171-234.

Bridge, J.S. (1993) The interaction between channel geometry, water flow, sediment transport and deposition in braided rivers. In: *Braided Rivers* (Eds J.L. Best and C.S. Bristow), *Geol. Soc., London, Special Publication*, **75(1)**, 13-71.

Bridge, J.S. (2006) Fluvial facies models: recent developments. In: *Facies Models Revisited* (Eds Posamentier, H.W. and Walker, R.G.), *Soc. Sed. Geol., Tulsa, OK, SEPM Spec. Pub.* **84**, 85-170.

Bridge, J.S., Collier, R. and Alexander, J. (1998) Large-scale structure of Calamus River deposits (Nebraska, USA) revealed using ground-penetrating radar. *Sedimentology*, **45**, 977-986.

Bristow, C.S. (1993) Sedimentary structures exposed in bar tops in the Brahmaputra River, Bangladesh. In: *Braided Rivers* (Eds J.L. Best and C.S. Bristow), *Geol. Soc., London, Spec. Pub.*, **75(1)**, 277-289.

Carling, P.A., Chateau, C.C., Leckie, D.A., Langdon, C.T., Scaife, R.G., and Parsons, D.R. (2015) Sedimentology of a tidal point-bar within the fluvial-tidal transition: River Severn Estuary, UK. In: *Fluvial-Tidal Sedimentology* (Eds P.J. Ashworth, J.L. Best and D.R. Parsons), *Dev. Sedimentol.*, **68**, 149-189.

Chaumillon, E., Bertin, X., Falchetto, H., Allard, J., Weber, N., Walker, P., Pouvreau, N., and Woppelmann, G. (2008) Multi time-scale evolution of a wide estuary linear sandbank, the Longe de Boyard, on the French Atlantic coast. *Mar. Geol.*, **251**, 209-223.

- Chaumillon, E., Fenies, H., Billy, J., Breilh, J.-F., and Richetti, H.** (2013) Tidal and fluvial controls on the internal architecture and sedimentary facies of a lobate estuarine tidal bar (The Plassac Tidal Bar in the Gironde Estuary, France). *Mar. Geol.*, **346**, 58-72.
- Chawla, A., Jay, D.A., Baptista, A.M., Wilkin, M., and Seaton, C.** (2008) Seasonal variability and estuary-shelf interactions in circulation dynamics of a river-dominated estuary. *Estuar. and Coast.*, **31**, 269-288.
- Choi, K.** (2010) Rhythmic climbing-ripple cross-lamination in inclined heterolithic stratification (IHS) of a macrotidal estuarine channel, Gomso Bay, west coast of Korea. *J. Sed. Res.*, **80**, 550-561.
- Choi, K.S., Dalrymple, R.W., Chun, S.S., and Kim, S.P.** (2004) Sedimentology of modern, inclined heterolithic stratification (IHS) in the macrotidal Han River delta, Korea. *J. Sed. Res.*, **74**, 677-689.
- Choi, K., Hong, C.M., Kim, M.H., Oh, C.R., and Jung, J.H.** (2013) Morphologic evolution of macrotidal estuarine channels in Gomso Bay, west coast of Korea: Implications for the architectural development of inclined heterolithic stratification. *Mar. Geol.*, **346**, 343-354.
- Clark, J.E. and Reinson, G.E.** (1990) Continuity and performance of an estuarine reservoir, Crystal Field, Alberta, Canada. In: *Sandstone Petroleum Reservoirs*, Springer, New York, NY, 343-361.
- Clark, S.M. and Snyder, G.R.** (1969) Timing and extent of flow reversal in the lower Columbia River. *J. Limnol. Oceanogr.*, **14**, 960-965.
- Dalrymple, R.W. and Choi, K.** (2007) Morphologic and facies trends through the fluvial-marine transition in tide-dominated depositional systems: A schematic framework for environmental and sequence-stratigraphic interpretation. *Earth-Sci. Rev.*, **81**, 135-174.
- Dalrymple, R.W. and Rhodes, R.N.** (1995) Estuarine dunes and bars. In: *Geomorphology and Sedimentology of Estuaries* (Eds G.M.E. Perillo), *Dev. Sedimentol.*, **53**, 359-422.
- Dalrymple, R.W., Zaitlin, B.A. and Boyd, R.** (1992) Estuarine facies models: conceptual basis and stratigraphic implications. *J. Sed. Petrol.*, **62(6)**, 1130-1146.
- Dalrymple, R.W., Mackay, D.A., Ichaso, A.A., and Choi, K.S.** (2012) Processes, morphodynamics, and facies of tide-dominated estuaries. In: *Principles of Tidal Sedimentology* (Eds R.A. Davis Jr. and R.W. Dalrymple), Springer, New York, 79-107.
- Dalrymple, R.W., Kurcinka, C.E., Jablonski, B.V.J., Ichaso, A.A. and Mackay, D.A.** (2015) Deciphering the relative importance of fluvial and tidal processes in the fluvial-marine transition. In: *Fluvial-Tidal Sedimentology* (Eds P.J. Ashworth, J.L. Best and D.R. Parsons), *Dev. Sedimentol.*, **68**, 3-45.

Durkin, P.R., Hubbard, S.M., Boyd, R.L. and Leckie, D.A. (2015) Stratigraphic expression of intra-point-bar erosion and rotation. *J. Sed. Res.*, **85**, 1238-1257.

Fain, A.M.V., Jay, D.A., Wilson, D.J., Orton, P.M. and Baptista, A.M. (2001) Seasonal and tidal monthly patterns of particulate matter dynamics in the Columbia River estuary. *Estuar. and Coast.*, **24(5)**, 770–786.

Feldman, H. and Demko, T. (2015) Recognition and prediction of petroleum reservoirs in the fluvial/tidal transition. In: *Fluvial-Tidal Sedimentology* (Eds P.J. Ashworth, J.L. Best and D.R. Parsons), *Dev. Sedimentol.*, **68**, 483-528.

Feldman, H., Mccrimmon, G. and De Freitas, T.A. (2008) Fluvial to estuarine valley-fill models without age-equivalent sandy shoreline deposits, based on the Clearwater Formation (Cretaceous) at Cold Lake, Alberta, Canada. In: *Recent Advances in Models of Siliciclastic Shallow-marine Stratigraphy, vol. 90* (Eds G.J. Hampson, R.J. Steel, P.M. Burgess and R.W. Dalrymple), Society for Sedimentary Geology (SEPM), Tulsa, OK, USA, 443-472.

Folk, R.L. and Ward W.C. (1957) Brazos River bar, a study in the significance of grain-size parameters. *J. Sediment. Petrol.*, **27**, 3-27.

Fox, D.S., Bell, S., Nehlsen, W. and Damron, J. (1984) The Columbia River Estuary: atlas of physical and biological characteristics. *Columbia River Data Development Program (CREDDP)*, Astoria, OR, 1-87.

Fustic, M., Hubbard, S.M., Spencer, R., Smith, D.G., Leckie, D.A., Bennett, B. and Larter, S. (2012) Recognition of down-valley translation in tidally influenced meandering fluvial deposits, Athabasca Oil Sands (Cretaceous), Alberta, Canada. *Mar. Petrol. Geol.*, **29**, 219-232.

Gelfenbaum, G. (1983) Suspended-sediment response to semidiurnal and fortnightly tidal variations in a mesotidal estuary: Columbia River, USA. *Mar. Geol.*, **52**, 39-57.

Gelfenbaum, G., Sherwood, C.R., Peterson, C.D., Kaminsky, G.M., Buijsman, M., Twichell, D.C., Ruggiero, P., Gibbs, A.E., and Reed, C. (1999) The Columbia River littoral cell - a sediment budget overview. In: *Coastal Sediments '99, Long Island, NY, 1999, Proc. Am. Soc. Civ. Eng.*, 1660-1675.

Ghinassi, M., D'alpaos, A., Gasparotto, A., Carniello, L., Brivio, L., Finotello, A., Roner, M., Franceschinis, E., Raldon, N., Howes, N. and Cantelli, A. (2018) Morphodynamic evolution and stratal architecture of translating tidal point bars: Inferences from the northern Venice Lagoon (Italy). *Sedimentology*, **65**, 1354-1377.

Goodwin, J.L., Emmett, E.W. and Glenne, B. (1970) Tidal study of three Oregon estuaries. Engineering Experimental Station, Oregon State University, Bull. No. 45, 1-32.

Graf, W.L. (2006) Downstream hydrologic and geomorphic effects of large dams on American rivers. *Geomorphology*, **79**, 336-360.

Grant, G.E., Schmidt, J.C. and Lewis, S.L. (2003) A geological framework for interpreting downstream effects of dams on rivers. In: *A Peculiar River* (Eds J.E. O'Connor and G.E. Grant), *Water Sci. App.*, **7**, 203-219.

Hamilton, P. (1990) Modelling salinity and circulation for the Columbia River estuary. *Prog. Oceanogr.*, **25**, 113-156.

Haushild, W.L.R., Perkins, W., Stevens, H.H., Dempster, G.R., Jr., and Glenn, J.L. (1966) Radionuclide transport in the pasco to Vancouver, Washington reach of the Columbia River July 1962 to September 1963. *U.S. Geological Survey Open File*, Portland, OR.

Hein, F.J. (2015) The Cretaceous McMurray oil sands, Alberta, Canada: A world-class, tidally-influenced fluvial-estuarine system – An Alberta government perspective. In: *Fluvial-Tidal Sedimentology* (Eds P.J. Ashworth, J.L. Best and D.R. Parsons), *Dev. Sedimentol.*, **68**, 561-621.

Herrman, R.B. (1972) *The distribution and abundance of clams in Grays Harbor as related to environmental conditions, summary report [unpub.]*, Longview, Washington, Weyerhaeuser Co.

Hickson, R. E. (1912) A report on the establishment of river gauges on lower Columbia River & Willamette Rivers. *Army Corps of Engineers*, 1-8.

Hoitink, A.J.F. and Jay, D.A. (2016) Tidal river dynamics: Implications for deltas. *Rev. Geophys.*, **54**, 240-272.

Horner-Devine, A.R., Jay, D.A., Orton, P.M., and Spahn, E.Y. (2009) A conceptual model of the strongly tidal Columbia River plume. *J. of Mar. Sys.*, **78**, 460-475.

Hubbard, S.M., Smith, D.G., Nielsen, H., Leckie, D.A., Fustic, M., Spencer, R.J. and Bloom, L. (2011) Seismic geomorphology and sedimentology of a tidally influenced river deposit, Lower Cretaceous Athabasca oil sands, Alberta, Canada. *AAPG Bull.*, **95**(7), 1123-1145.

Jablonski, B.V.J. and Dalrymple, R.W. (2016) Recognition of strong seasonality and climatic cyclicity in an ancient, fluvially dominated, tidally influenced point bar: Middle McMurray Formation, Lower Steepbank River, north-eastern Alberta, Canada. *Sedimentology*, **63**, 552-585.

Jay, D.A. (1984) Circulatory processes in the Columbia River Estuary. CREST, Astoria, Oregon, 1-169.

Jay, D.A. (2009) Evolution of tidal amplitudes in the eastern Pacific Ocean. *Geophys. Res. Lett.*, **36**, L04603, doi:10.1029/2008GL036185.

Jay, D.A. and Naik, P.K. (2011) Distinguishing human and climate influences on hydrological disturbance processes in the Columbia River, USA. *Hydrolog. Sci. J.*, **56**, 1186-1209.

Jay, D.A., Giese, B.S. and Sherwood, C.R. (1990) Energetics and sedimentary processes in the Columbia River Estuary. *Prog. Oceanogr.*, **25**, 157-174.

Jay, D.A., Leffler, K. and Degens, S. (2011) Long-term evolution of Columbia River tides. *J. Waterway, Port, Coastal, and Ocean Eng.*, **137**(4), 182-191.

Johnson, J.W. (1972) Tidal inlets on the California, Oregon, and Washington coasts. Hydraulic Engineering Laboratory, University of California, Berkeley, *Technical Report HEL 24-12*.

Johnson, S.M. and Dashtgard, S.E. (2014) Inclined heterolithic stratification in a mixed tidal-fluvial channel: Differentiating tidal versus fluvial controls on sedimentation. *Sed. Geol.*, **301**, 41-53.

Knotts, N.P. and Barrick, R.C. (1976) Hydrodynamics of Grays Harbor estuary, Washington: Appendix A. In: *Maintenance dredging and the environment of Grays Harbor, Washington*. U.S. Army Engineer District, Seattle, Washington, 1-95.

Kukulka, T. and Jay, D.A. (2003) Impacts of Columbia River discharge on salmonoid habitat: 1. A nonstationary fluvial tide model. *J. Geophys. Res.*, **108**(C9), 3293, doi:10.1029/2002JC001382.

Leeder, M. and Bridges, P.H. (1975) Flow separation in meander bends. *Nature*, **253**, 338-339.

Leuven, J.R.F.W., Kleinhans, M.G., Weisscher, S.A.H. and van der Vegt, M. (2016) Tidal sand bar dimensions and shapes in estuaries. *Earth-Sci. Rev.*, **161**, 204-223.

Losada, M.A., Díez-Minguito, M. and Reyes-Merlo, M.Á. (2017) Tidal-fluvial interaction in the Guadalquivir River Estuary: Spatial and frequency-dependent response of currents and water levels. *J. Geophys. Res. Oceans*, **122**, 847-865.

Martinius, A.W. and Van den Berg, J.H. (2011) *Atlas of sedimentary structures in estuarine and tidally-influenced river deposits of the Rhine-Meuse-Scheldt system: their application to the interpretation of analogous outcrop and subsurface depositional systems*. EAGE Publications, Houten, The Netherlands, 298 pp.

Martinius, A.W., Jablonski, B.V.J., Fustic, M., Strobl, R. and Van den Berg, J.H. (2015) Fluvial to tidal transition zone facies in the McMurray Formation (Christina River, Alberta, Canada), with emphasis on the reflection of flow intensity in bottomset architecture. In: *Fluvial-Tidal Sedimentology* (Eds P.J. Ashworth, J.L. Best and D.R. Parsons), *Dev. Sedimentol.*, **68**, 445-480.

Moreton, D.J. and Carter, B.J. (2015) Characterizing alluvial architecture of point bars within the McMurray Formation, Alberta, Canada, for improved bitumen resource prediction and recovery. In: *Fluvial-Tidal Sedimentology* (Eds P.J. Ashworth, J.L. Best and D.R. Parsons), *Dev. Sedimentol.*, **68**, 529-559.

Mumpy, A.J., Jol, H.M., Kean, W.F. and Isbell, J.L. (2007) Architecture and sedimentology of an active braid bar in the Wisconsin River based on 3-D ground penetrating radar. In: *Stratigraphic Analysis Using GPR* (Eds G.S. Barker and H.M. Jol), *Geol. Soc. Am. Spec. Pap.* **432**, 111-131.

Mutti, E., Rosell, J., Allen, G.P., Fonnesu, F. and Sgavetti, M. (1985) The Eocene Baronia tide dominated delta-shelf system in the Ager Basin. In: *Excursion Guidebook: 6th International Association of Sedimentologists European Regional Meeting*, 577–600.

Naik, P.K. and Jay, D.A. (2005) Estimation of Columbia River virgin flow: 1879 to 1928. *Hydrol. Process.*, **19**, 1807-1824.

Naik, P.K. and Jay, D.A. (2011) Distinguishing human and climate influences on the Columbia River: Changes in mean flow and sediment transport. *J. Hydrol.*, **404**, 259-277.

Nanson, G.C., and Page, K.J. (1983) Lateral accretion of fine-grained concave benches on meandering rivers. In: *Modern and Ancient Fluvial Systems* (Eds D.J. Collinson and J. Lewin), *Int. Assoc. Sedimentol. Spec. Publ.* **6**, 133-143.

Parker, N.O., Sambrook Smith, G.H., Ashworth, P.J., Best, J.L., Lane, S.N., Lunt, I.A., Simpson, C.J. and Thomas, R.E. (2013) Quantification of the relation between surface morphodynamics and subsurface sedimentological product in sandy braided rivers. *Sedimentology*, **60**, 820-839.

Percy, K.L., Sutterlin, C., Bella, D.A. and Klingeman, P.C. (1974) Oregon's Estuaries: Sea Grant College Program. Oregon State University, Corvallis, 1-294.

Peterson, C., Scheidegger, K., Komar, P. and Niem, W. (1984) Sediment composition and hydrography in six high-gradient estuaries of the northwestern United States. *J. Sed. Petrol.*, **54**, 86-97.

Peterson, C.D., Gates, E.B., Minor, R. and Baker, D.L. (2013) Accommodation space controls on the latest Pleistocene and Holocene (16-0 ka) sediment size and bypassing in the lower Columbia River valley: a large fluvial-tidal system in Oregon and Washington, USA. *J. Coast. Res.*, **29** (5), 1191–1211.

Peterson, C., Vanderburgh, S., and Roberts, M.C. (2014) Late Holocene geomorphology of the Columbia River estuary, Oregon and Washington, USA. *J. Geogr. Geol.*, **6**(2), 1-27.

Prokocki, E.W., Best, J.L., Ashworth, P.J., Parsons, D.R., Sambrook Smith G.H., Nicholas, A.P., Simpson, C.J., Wang, H., Sandbach, S.D. and Keevil, C.E. (2015) Mid to late Holocene geomorphological and sedimentological evolution of the fluvial-tidal zone: Lower Columbia

River, WA/OR, USA. In: *Fluvial-Tidal Sedimentology* (Eds P.J. Ashworth, J.L. Best and D.R. Parsons), *Dev. Sedimentol.*, **68**, 193-226.

Reesink, A.J.H., Ashworth, P.J., Sambrook Smith, G.H., Best, J.L., Parsons, D.R., Amsler, M.L., Hardy, R.J., Lane, S.N., Nicholas, A.P., Orfeo, O., Sandbach, S.D., Simpson, C.J. and Szupiany, R.N. (2014) Scales and causes of heterogeneity in bars in a large multi-channel river: Río Paraná, Argentina. *Sedimentology*, **61**, 1055-1085.

Reijnenstein, H.M., Posamentier, H.W. and Bhattacharya, J.P. (2011) Seismic geomorphology and high-resolution seismic stratigraphy of inner-shelf fluvial, estuarine, deltaic, and marine sequences, Gulf of Thailand. *AAPG Bull.*, **95(11)**, 1959-1990.

Rubin, D.M., Topping, D.J., Schmidt, J.C., Hazel, J., Kaplinski, M. and Melis, T.S. (2002) Recent sediment studies refute Glen Canyon Dam hypothesis. *EOS*, **83(25)**, 273-278.

Sambrook Smith, G.H., Ashworth, P.J., Best, J.L., Woodward, J. and Simpson, C.J. (2006) The sedimentology and alluvial architecture of the sandy braided South Saskatchewan River, Canada. *Sedimentology*, **53**, 413-434.

Sambrook Smith, G.H., Ashworth, P.J., Best, J.L., Lunt, I.A., Orfeo, O. and Parsons, D.R. (2009) The sedimentology and alluvial architecture of a large braid bar, Río Paraná, Argentina. *J. Sed. Res.*, **79**, 629-642.

Sandbach, S.D., Nicholas, A.P., Ashworth, P.J., Best, J.L., Keevil, C.E., Parsons, D.R., Prokocki, E.W. and Simpson, C.J. (2018) Hydrodynamic modelling of tidal-fluvial flows in a large river estuary. *Estuar. Coast. Shelf. Sci.*, **212**, 176-188.

Schmidt, J.C. and Graf, B. (1990) Aggradation and degradation of alluvial-sand deposits, 1965 to 1986, Colorado River, Grand Canyon National Park, Arizona. *USGS Prof. Pap.* 1493.

Seminara G., Lanzoni S., Pittaluga M.B. and Solari, L. (2001) Estuarine patterns: an introduction to their morphology and mechanics. In: *Geomorphological Fluid Mechanics* (Eds N.J. Balmforth and A. Provenzale), *Lecture Notes in Physics*, **582**, Springer, Berlin, Heidelberg.

Shanley, K.W., McCabe, P.J. and Hettlinger, R.D. (1992) Tidal influence in Cretaceous fluvial strata from Utah, USA: a key to sequence stratigraphic interpretation. *Sedimentology*, **39**, 905-930.

Shanmugam, G., Poffenberger, M. and Toro Alava, J. (2000) Tide-dominated estuarine facies in the Hollin and Napo. *AAPG Bull.*, **84(5)**, 652-682.

Sherwood, C.R. and Creager, J.S. (1990) Sedimentary geology of the Columbia River Estuary. *Prog. Oceanogr.*, **25**, 15-79.

Sherwood, C.R., Jay, D.A., Harvey, R.B., Hamilton, P. and Simenstad, C.A. (1990) Historical changes in the Columbia River Estuary. *Prog. Oceanogr.*, **25**, 299-352.

Simenstad, C.A., Burke, J.L., O'Connor, J.E., Cannon, C., Heatwolve, D.W., Ramiez, M.F., Waite, I.R., Counihan, T.D. and Jones, K.L. (2011) Columbia River estuary ecosystem classification—concept and application. U.S. Geological Survey, open-file report 2011-1228, Reston, 1-54.

Sisulak, C.F. and Dashtgard, S.E. (2012) Seasonal controls on the development and character of inclined heterolithic stratification in a tide-influenced, fluvially dominated channel: Fraser River, Canada. *J. Sed. Res.*, **82**, 244-257.

Smith, D.G. (1987) Meandering river point bar lithofacies models: modern and ancient examples compared. In: *Recent Developments in Fluvial Sedimentology* (Eds F.G. Ethridge, R.M. Flores and M.D. Harvey), *Soc. Econ. Paleontol. Mineral. Spec. Publ.*, **39**, 83-91.

Smith, D.G. (1988) Tidal bundles and mud couplets in the McMurray Formation, northeastern Alberta, Canada. *Bull. Can. Petrol. Geol.*, **36**, 216-219.

Smith, D.G. (1989) Comparative sedimentology of mesotidal (2 to 4 m) estuarine channel point bar deposits from modern examples and ancient Athabasca Oil Sands (Lower Cretaceous), McMurray Formation. In: *Modern and Ancient Examples of Clastic Tidal Deposits – Core and Peel Workshop* (Eds G.E. Reinson), *Can. Soc. Petrol. Geol.*, Second International Research Symposium on Clastic Tidal Deposits, 60-65.

Smith, D.G., Hubbard, S.M., Leckie, D.A. and Fustic, M. (2009) Counter point-bar deposits: lithofacies and reservoir significance in the meandering modern Peace River and ancient McMurray Formation, Alberta, Canada. *Sedimentology*, **56**, 1655-1669.

Smith, D.G., Hubbard, S.M., Lavigne, J.R., Leckie, D.A. and Fustic, M. (2011) Stratigraphy of counter-point-bar and eddy-accretion deposits in low-energy meander belts of the Peace-Athabasca Delta, northeast Alberta, Canada. In: *From River to Rock Record: The Preservation of Fluvial Sediments and Their Subsequent Interpretation* (Eds S. Davidson, S. Leleu and C.P. North), *SEPM Spec. Publ.*, **97**, 143-152.

Stolz, A., Martin, C. and Wong, C. (2005) Vertical control in a tidally influenced complex river system with a fixed low water datum. *Hydrographic Society of America Meeting*, 20-31.

Templeton, W.J. and Jay, D.A. (2013) Lower Columbia River sand supply and removal: estimates of two sand budget components. *J. Water. Port Ocean Eng.*, **139**(5), 383-392.

Thomas, R.G., Smith, D.G., Wood, J.M., Visser, J., Calverley-Range, E.A. and Koster, E.H. (1987) Inclined heterolithic stratification – terminology, description, interpretation and significance. *Sed. Geol.*, **53**, 123-179.

Topping, D. J., Rubin, D. M. and Vierra Jr., L. E. (2000a) Colorado River sediment transport. 1. Natural sediment supply limitation and the influence of Glen Canyon Dam. *Wat. Resour. Res.*, **36**(2), 515-542.

Topping, D. J., Rubin, D. M., Nelson, J. M., Kinzel III, P. J. and Corson, I. C. (2000b) Colorado River sediment transport. 2. Systematic bed-elevation and grain-size effects of sand supply limitation. *Wat. Resour. Res.*, **36(2)**, 543-570.

Utt, M.E. (1975) *Seasonal variations in tidal dynamics, water quality and sediments in the Siuslaw Estuary. [M.Sc. thesis].* Oregon State University, 76 pp.

Van de Lageweg, W.I. and Feldman, H. (2018) Process-based modelling of morphodynamics and bar architecture in confined basins with fluvial and tidal currents. *Mar. Geol.*, **398**, 35-47.

Van de Lageweg, W.I., Braat, L., Parsons, D.R. and Kleinhans, M.G. (2018) Controls on mud distribution and architecture along the fluvial-to-marine transition. *Geology*, **46**, 971-974.

Van den Berg, J.H., Boersma, J.R. and Van Gelder, A. (2007) Diagnostic sedimentary structures of the fluvial-tidal transition zone: evidence from deposits of the Rhine Delta. *Nether. J. Geosci.*, **86(3)**, 287-306.

Walton, Jr., T.L. and Adams, W.D. (1976) Capacity of inlet outer bars to store sand. *Proc. Am. Soc. Civ. Eng. Part II: Coastal Sediment Problems*, 1919-1937.

Wightman, D.M. and Pemberton, S.G. (1997) The Lower Cretaceous (Aptian) McMurray Formation: an overview of the Fort McMurray area, northeastern Alberta. In: *Petroleum Geology of the Cretaceous Mannville Group, Western Canada* (Eds S.G. Pemberton and D.P. James), *Can. Soc. Petrol. Geol. Mem.*, **18**, 312–344.

Wightman, D.M., Strobl, R.S., Cotterill, D.K., Berhane, H., and Attalla, M.N. (1997) Stratigraphy, depositional modelling and resource characterization of the McMurray/Wabiskaw deposit, western portion of the Athabasca oil sands area, northeastern Alberta. In: *Petroleum Geology of the Cretaceous Mannville Group, Western Canada* (Eds S.G. Pemberton and D.P. James), *Can. Soc. Petrol. Geol. Mem.*, **18**, 345-374.

Williams, G.P. and Wolman, M.G. (1984) Downstream effects of dams on alluvial rivers. *USGS Prof. Pap. 1286*, Washington, D.C.

Yalin, M.S. (1964) Geometrical properties of sand waves. *J. Hydraul. Eng.*, **90(5)**, 105–119.

TABLE LEGEND

Table 1. Comparison of modern fluvio-tidal characteristics and hydrographic ratios (H_g) of rivers and tidal-bays located along the central Cascadia Margin, USA. Note $H_g =$

$(Q_{tide}/Q_{Wavg}) \times 6hrs$ (half a tidal-cycle), and that values of $H_g < 10$ represent systems that are fluvially, or ebb-tidal, dominant. Modified from Peterson *et al.* (1984).

Table 2. Ground penetrating radar (GPR) reflector facies descriptions and examples captured in LCR mid-channel barform profiles. See main text for specific FTT hydraulic regime sedimentological descriptions and interpretations.

Table 3. Key to vibracore sedimentary logs and GPR cross-sectional profiles. The Mean Higher-High Water (MHHW), Mean Sea Level (MSL), and Mean Lower-Low Water (MLLW) levels displayed on each log and GPR-profile were determined from Stolz *et al.* (2005). Note that the potential maximum depths of LCR intrabasinal wind-wave sediment resuspension (MaxW1 and MaxW2) are from Peterson *et al.* (2014).

FIGURE LEGEND

Figure 1. Schematic depositional model of Inclined Heterolithic Stratification (IHS) within point-bars of a hypothetical FTT as tidal-processes increase in magnitude and frequency in the downstream-direction. This model assumes that the increased deposition of relatively thick silt/mud horizons within point-bar accretion-sets is primarily the product of suspension-fallout of fine-grained sediment during tidal slackwater periods, and enhanced flocculation and deposition of fines within the turbidity-maximum zone. Modified from Smith (1987).

Figure 2. (A) Aerial image of the lower Columbia River (LCR) study reach displaying the mean boundaries of the FTT hydraulic regimes as defined by Jay *et al.* (1990) as well as the outline of the main navigation channel (dashed white line). Included are the positions of the three mid-channel barforms investigated herein (yellow rectangles), the longitudinal channel extent of salinity intrusion during high- and low- fluvial flows as reported by Fox *et al.* (1984) and Chawla *et al.* (2008), the average position of the LCR turbidity-maximum (green stars) at ~ rkm 21 (Jay

et al., 1990), and the location of the Beaver (Port Westward) gauge station at rkm 85. (B-D) magnified images of the three bars analysed herein displaying the locations where ground penetrating radar (GPR) transects (yellow lines) and sediment cores (pink circles) were collected. Aerial imagery from US National Agriculture Imagery Program (NAIP) at <https://gdg.sc.egov.usda.gov/>.

Figure 3. (A) Monthly averaged ‘natural’ LCR discharge (1879-1899; blue line) vs monthly averaged irrigation depleted and dam regulated modern LCR discharge (1970-2004; purple line) at the Port Westward (Beaver) gauge station at rkm 85 positioned at the upstream boundary of study reach. Modified from Naik & Jay (2011). (B) Planform diagram of the LCR from rkm 0-235 displaying the boundaries of its FTT regimes as well as the limits and positions of pertinent tidal-characteristics. Also shown is: i) the modern LCR water surface profile from rkm 0-235 at extreme high-river flow and at low-river flow and low-tide, and ii) thalweg grain size range.

Figure 4. (A) Mean energy flux divergence of LCR tidal (pink line) vs fluvial (purple line) hydraulic sources as computed by Giese & Jay (1989) and Jay *et al.* (1990). Note that the summation of tidal- and fluvial- energy fluxes equals the total amount of energy flux across channel cross-sections at each LCR rkm as measured by Jay (1984). (B) Annual LCR intrabasinal wind-wave directions and magnitudes relative to the positions of Bars CB1-S and CB2-W. Note, however, that the image displayed was taken when water-levels were below the Mean Lower Low Water (MLLW) mark, and that the normal condition is for almost all barforms displayed to be submerged when the water surface is higher than MLLW (see figure 6.1, Prokocki *et al.*, 2015). The largest wind-waves (pink arrows) are generated over the longest fetch length between January-April and in October and November, and are oriented from the west-southwest to east-northeast, whilst smaller wind-waves (white arrows) are produced from May to September, and are oriented from north-northwest to south-southeast. Wind data from Peterson *et al.* (2014).

Figure 5. (A) Temporally averaged relative energy diagram for the LCR FTT study reach investigated. The MTFR (Bars CB1-S and CB2-W) is mainly subjected to fluvial-currents during moderate- to high- river stages, but at low-river stage will experience combined-flows composed of fluvial- and/or tidal- currents and intrabasinal wind-wave oscillatory-currents. Next, within the FDTIR (Bar BT1-P), sediment transport is primarily dictated by fluvial-currents as the result of moderate- to high- river stages. This diagram is based from the results of Jay *et al.* (1990) and Peterson *et al.* (2014). (B) Hindcast estimates (1879-1985) of LCR mean annual sediment load (Q_s), and sand fraction ($Q_{sand} > 0.062\text{mm}$), at rkm 172 given by the discharge- Q_s rating-curve of Sherwood *et al.* (1990). Note that these estimates exclude the sediment contributions of the Willamette and Cowlitz Rivers. Also provided are the: i) Holocene averaged (\sim last 10,000 yrs) estimates of LCR Q_s conveyed to the lower Columbia River Valley (LCRV; grey rectangle) and amount utilized to fill the LCRV to its present level (blue rectangle), and ii) estimations of the pre-1900 (black dashed line), 1964-1970 (purple line), and post-1980 (pink dashed line) LCR Q_s . Modified from Sherwood *et al.* (1990).

Figure 6. (A-C) Time sequenced aerial imagery displaying the initial development of Bars BT1-P, CB1-S, and CB2-W, in 1990, and their subsequent migration patterns to 2011/2012, relative to GPR-profiles (yellow lines) and vibracores (pink circles) collected in 2011 (Bars BT1-P and CB1-S) and 2013 (Bar CB2-W), respectively. Reported average migration rates were estimated over the time period 1990-2011 (Bar BT1-P), and 1990-2012 (Bars CB1-S and CB2-W). Note that average migration rates represent the measured straight line distance between the 1990 centre of each bar and its new centre position in 2011, or 2012. Thus, average migration rates are not partitioned into their lateral- and longitudinal- oriented components of translation, and represent overall spatio-temporal movement. Lastly, all bars investigated formed within less human affected secondary channels located away from the consistently dredged main navigation

channel (see also Fig. 2 for channel and bar locations). Aerial imagery from US National Agriculture Imagery Program (NAIP) at <https://gdg.sc.egov.usda.gov/>.

Figure 7. Sedimentary logs, and vertical D_{50} grain size and sediment sorting index trends of the three vibracores collected from Bar BT1-P. Cores are presented from downstream (bartail; core BT1-P3) to upstream (barhead; core BT1-P1). Also marked are the depth intervals that represent the sedimentology and depositional fabric of coupled radar facies. See Table 3 for key to core logs, and Figure 8 for vibracore locations.

Figure 8. Interpreted GPR-profiles from Bar BT1-P positioned within the FDTIR. Profiles display the alluvial architecture of Bar BT1-P as comprising the three major radar facies (1-3; colour coded as in Table 2) identified in this study. Also shown are the locations of vibracores collected along each profile (cores BT1-P2 and BT1-P3). Note the overall dominance of radar facies 3.

Figure 9. Core logs, vertical D_{50} grain size, and sediment sorting index trends, of the three vibracores collected from Bar CB1-S. Cores are presented from downstream (bartail; core CB1-S1) to upstream (barhead; core CB1-S2). Demarcated are the depth intervals representing sediments preserved from associated radar facies, and maximum depth windows of potential wind-wave influence. See Table 3 for key to logs, and Figure 10 for vibracore locations.

Figure 10. Interpreted GPR-profiles from Bar CB1-S located within the MTFR, which display the sedimentary architecture of this bar with respect to preserved radar facies. Also shown are the locations of shallow vibracores collected along each profile (cores CB1-S1, CB1-S2, and CB1-S3), and the colour-coded radar facies. Note the dominant preservation of radar facies 1 and 3.

Figure 11. Sedimentary logs, vertical D_{50} grain size, and sediment sorting index trends, of the three vibracores collected from Bar CB2-W. Cores are presented from downstream (bartail; core CB2-W4) to upstream (barhead; core CB2-W1). Also marked are the depth intervals representing the sedimentology and depositional fabric of coupled radar facies, and maximum

depth windows of potential wind-wave influence. See Table 3 for key to logs, and Figure 12 for vibracore locations.

Figure 12. Interpreted GPR-profiles from Bar CB2-W positioned within the MTR. Profiles display the preserved stacking patterns of radar facies within Bar CB2-W. The locations of vibracores collected along each profile (cores CB2-W1, CB2-W3, and CB2-W4) are also shown, together with the colour-coded radar facies. Similar to Bar CB1-S, note the dominant preservation of radar facies 1 and 3.

Figure 13. (A) Areal occurrences of radar facies within each of the thirteen GPR-transects from Bar BT1-P. This bar is dominated by facies 3 with minimal occurrence of facies 1a and 2a. The occurrence of facies 1a is nearly always constrained to bar-tail downstream-extension (lines PY1, PY3, and PY4), whilst facies 2a is mainly confined to bar-margin lateral-accretion (lines PX4-PX9). (B) Calculated occurrence of radar facies within Bar BT1-P GPR-transects with respect to depth. Notice the dominance of facies 3 (> 80%) throughout all depth intervals.

Figure 14. (A) Spatial distributions of radar facies areal occurrences within the twelve GPR-profiles at Bar CB1-S. This bar is dominated by facies 1b, with notable occurrence of facies 2a and 3. Preservation of facies 2a is typically restricted to bar-margin lateral-accretion (lines SX1, SX2, SX7, and SX8), whereas facies 3 is found in variable occurrence within all longitudinal- and lateral- transects. (B) Occurrence of Bar CB1-S radar facies with respect to depth. Note that the preservation of facies 3 dominates from 4-7m depth ($\geq 60\%$; below potential wind-wave influence), whilst between 0-4m depth (within potential wind-wave influence) facies 1b ($\geq 55\%$) dominates, as facies 2a and 3 diminish to < 25%.

Figure 15. (A) Areal occurrence of radar facies within the seventeen GPR-transects at Bar CB2-W. This bar primarily comprises facies 1c, 2b and 3, with lower preservation of any style of facies 1 relative to Bar CB1-S. Note that occurrence of facies 2b represents: i) bar-margin lateral-accretion (lines WX6, WX8, WX9, and WX11-WX13), and ii) downstream-oriented bartail-limb accretion (lines WY1 and WY4). (B) Occurrences of Bar CB2-W radar facies with respect to depth. Notice also that the preservation of facies 3 dominates from 3-7m depth ($\geq 60\%$), whereas

between 0-2m depth (within shallowest zone of potential wind-wave influence) facies 1c ($\geq 60\%$) dominates as facies 3 diminishes to $< 25\%$. However, unlike Bar CB1-S, facies 2 (in the form of 2b) is more abundant ($\sim 8-15\%$ in occurrence) within the 0-3m depth interval.

Figure 16. Schematic representations of the different styles, depositional fabrics, and positions, of preserved IHS within LCR FTT mid-channel barforms experiencing differing hydraulic processes and sediment transport conditions. (A) IHS is formed primarily during high-river stage events when LCR suspended-sediment concentrations are highest, where fines can be trapped, and deposited, within side-bar and bartail low-velocity recirculation cells. (B) IHS is produced by the redistribution of fines (especially bartail fines) deposited during high-river stage(s) by frequent strong wind-waves + bidirectional tidal-currents at low-river stages. Ebb-tidal currents may carry wind-wave induced resuspended fines downstream, whilst flood-tidal currents and associated slackwater periods may transport and deposit wind-wave induced resuspended fines into mid-bar and barhead accretion-sets. (C) Bartail IHS forms during high-river stage(s) in same method as (A), but during low-river stage, more infrequent weaker wind-waves do not resuspend as many fines, which allows for IHS production from bartail to barhead that is derived from a combination of high river-stage deposited fines and those deposited during tidal slackwater intervals. Note that all IHS within (C) is bioturbated due to weaker wind-wave energy.

Figure 17. Plots of barhead to bartail vibracore D_{50} grain size and sediment sorting trends for the three LCR mid-channel barforms analysed. (A) Bar BT1-P (FDTIR) displays a fining-upwards trend from its barhead to bartail. (B) Barhead to bartail deposits of Bar CB1-S (MTFR) fine-upward then coarsen- and sort- upward within MaxW1 at $\sim 1.5\text{m}$ depth. (C) Bar CB2-W (MTFR) barhead to bartail alluvium fine-upward then coarsen-upward at $\sim 1\text{m}$ depth, but do not sort-upward until near the top of MaxW1 at $\sim 0.5\text{m}$ depth. See Table 3 for definitions of abbreviated labels and sediment sorting classifications.

Figure 18. (A) Time-sequenced schematic diagram in longitudinal cross-sectional view depicting the architectural and sedimentological evolution of a LCR barform within the MTFR that is affected by frequent and strong intrabasinal wind-waves during low-river stage. (B) Time-sequenced schematic diagram in longitudinal cross-sectional view displaying the architectural

and sedimentological evolution of a LCR barform within the MTFR that is weakly, or sporadically, influenced by intrabasinal wind-waves during low-river stage.

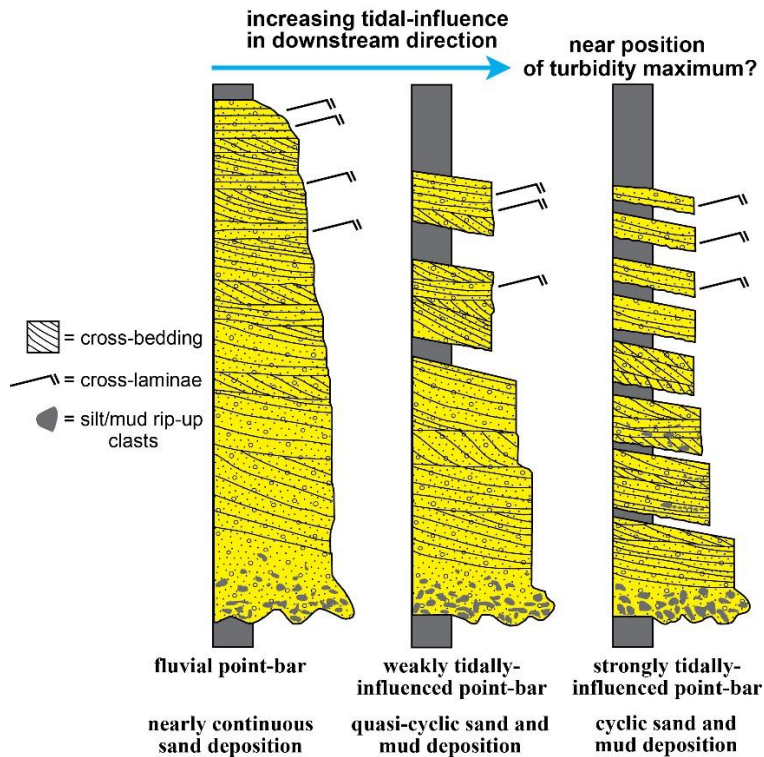


Fig. 1. Schematic depositional model of the favoured development in Inclined Heterolithic Stratification (IHS) within point-bars of a hypothetical FTT as tidal-processes increase in magnitude and frequency in the downstream-direction. Note that this model assumes that the increased deposition of relatively thick silt/mud horizons within point-bar accretion-sets is primarily the product of suspension-fallout of fine-grained sediment during tidal slackwater periods, and enhanced flocculation and deposition of fines within the zone of turbidity-maximum development. Modified from Smith (1987).

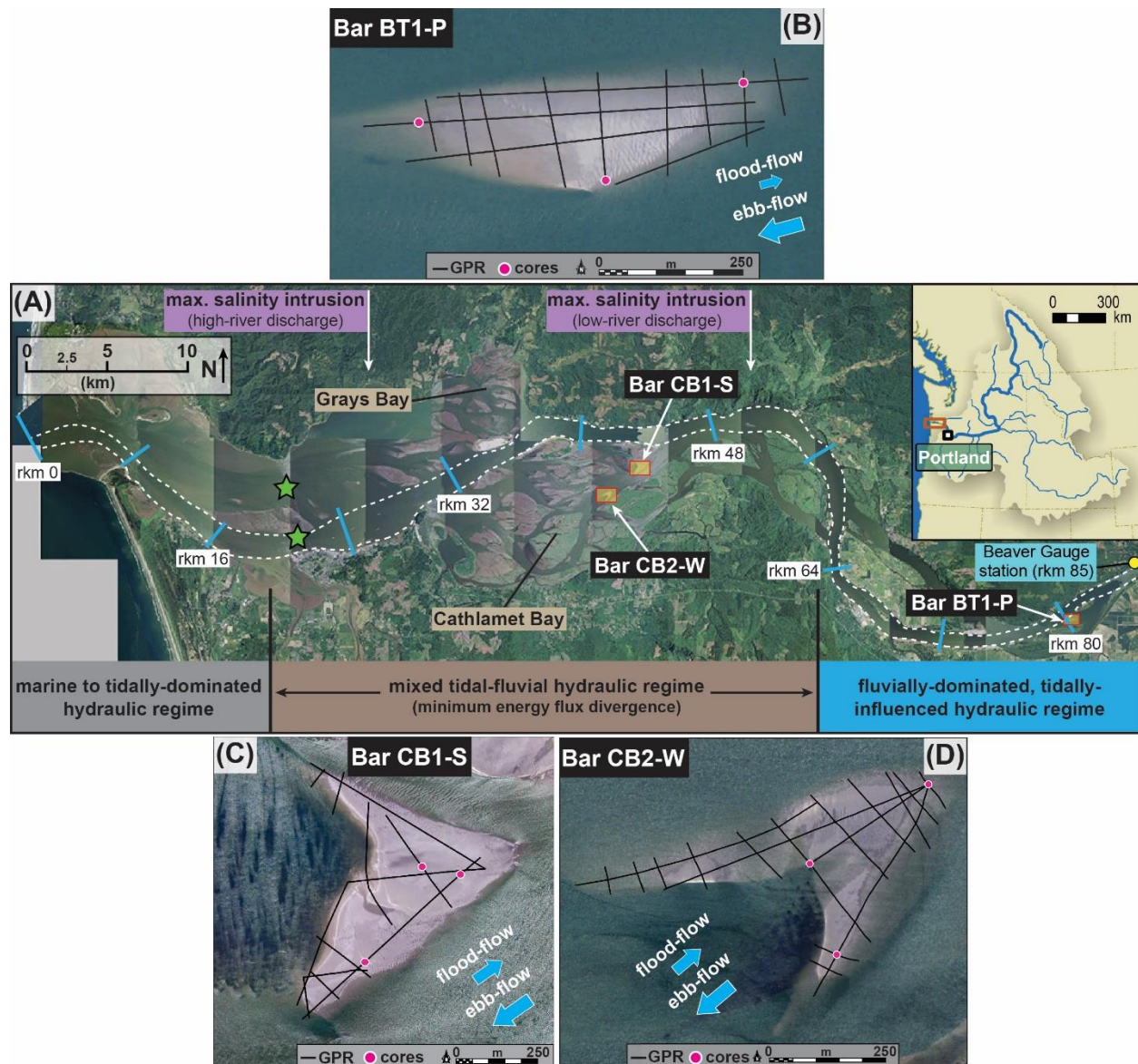


Fig. 2. Aerial image of the lower Columbia River (LCR) study reach displaying the mean boundaries of the FTT hydraulic regimes as defined by Jay *et al.* (1990) as well as the outline of the main navigation channel (dashed white line). Included are the positions of the three mid-channel barforms investigated (yellow rectangles), and magnified images (B-D) of these bars displaying the locations where ground penetrating radar (GPR) transects (black lines) and sediment cores (pink circles) were collected. Also shown is the longitudinal channel extent of salinity intrusion during high- and low- fluvial flows as reported by Fox *et al.* (1984) and Chawla *et al.* (2008), the average position of the LCR turbidity-maximum (green stars) at ~ rkm 21 (Jay *et al.*, 1990), and the location of the Port Westward (Beaver) gauge station at rkm 85. Aerial imagery from US National Agriculture Imagery Program (NAIP) at <https://gdg.sc.egov.usda.gov/>.

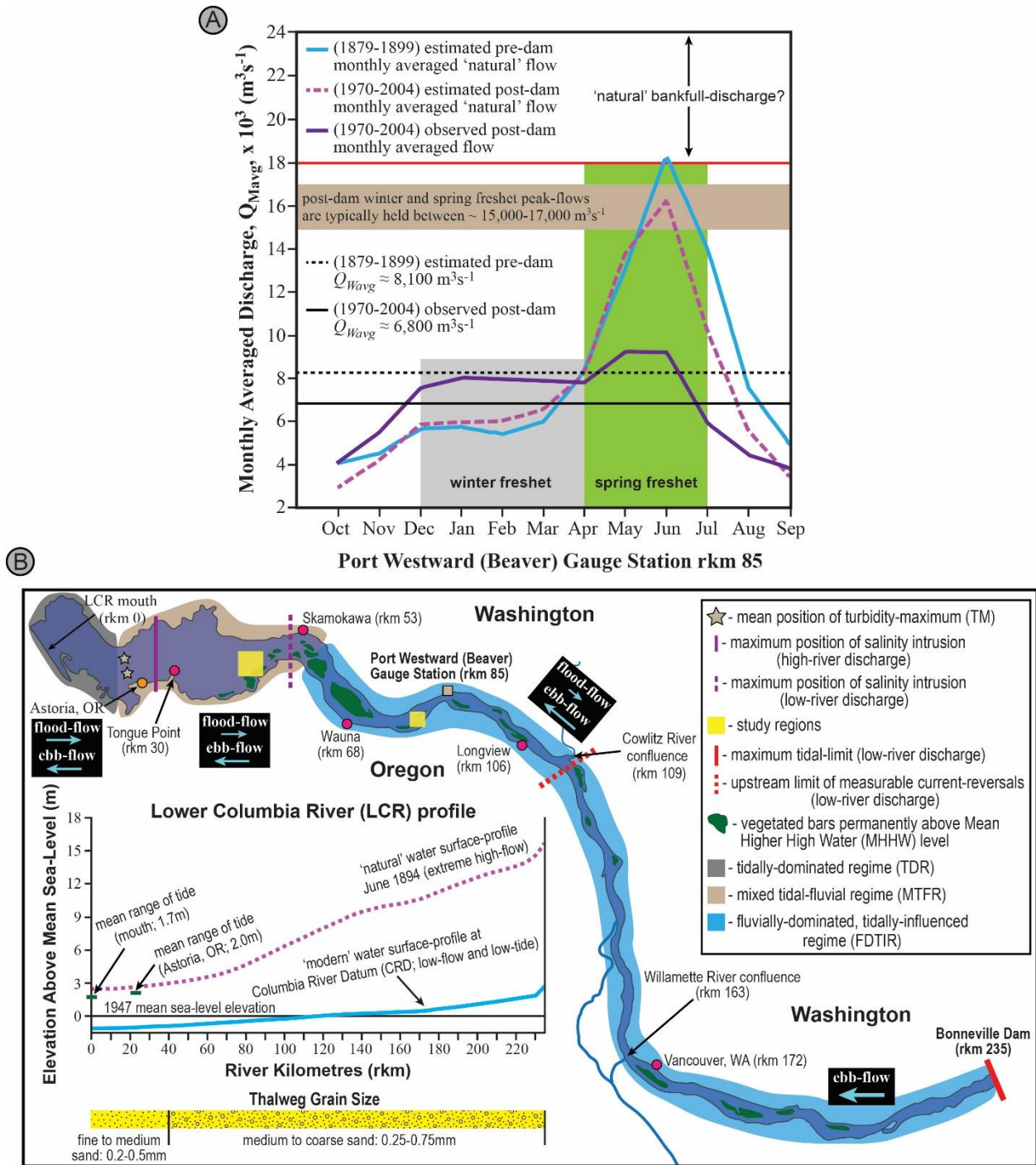


Fig. 3. (A) Monthly averaged 'natural' LCR discharge (1879-1899; blue line) vs monthly averaged irrigation depleted and dam regulated modern LCR discharge (1970-2004; purple line) at the Port Westward (Beaver) gauge station at rkm 85 positioned at the upstream boundary of study reach. Modified from Naik & Jay (2011). (B) Planform diagram of the LCR from rkm 0-235 displaying the boundaries of its FTT regimes as well as the limits and positions of pertinent tidal-characteristics. Also shown is: i) the modern LCR water surface profile from rkm 0-235 at extreme high-river flow and at low-river flow and low-tide, and ii) thalweg grain size range.

| | Grays Harbor/Chehalis River | Tillamook Bay | Siuslaw River | Alesea River | Siletz River | Lower Columbia River |
|--|-----------------------------|-----------------------|-----------------------|-----------------------|-----------------------|------------------------|
| mean annual fluvial discharge, Q_{Wavg} , at mouth (m^3s^{-1}) | 320 (b) | 60 (f) | 89 (f) | 43 (f) | 55 (f) | 7,300 (h) |
| mean diurnal tidal prism, Q_{tide} , at mouth (m^3) | 6.0×10^8 (e) | 6.1×10^7 (d) | 1.0×10^7 (f) | 1.4×10^7 (a) | 9.9×10^6 (a) | 11.0×10^8 (c) |
| mean range of tide at, or near, mouth (m) | 2.2 (e) | 1.7 (d) | 1.6 (i) | 1.8 (a) | 1.5 (d) | 1.7 (j) |
| mean hydrographic ratio (H_g) | 86 (g) | 47 (g) | 5 (g) | 15 (g) | 8 (g) | 7 |

- (a) Goodwin *et al.* (1970)
- (b) Hermann (1972)
- (c) Walton & Adams (1976)
- (d) Johnson (1972)
- (e) Knotts & Barrick (1976)
- (f) Percy *et al.* (1974)
- (g) Peterson *et al.* (1984)
- (h) Naik & Jay (2011)
- (i) Utt (1975)
- (j) Simenstad *et al.* (2011)

Table 1. Comparison of modern fluvio-tidal characteristics and hydrographic ratios (H_g) of rivers and tidal-bays located along the central Cascadia Margin, USA. Note $H_g = (Q_{tide}/Q_{Wavg}) \times 6hrs$ (half a tidal-cycle), and that values of H_g approaching unity (< 10) represent systems that are fluvially, or ebb-tidal, dominant. Modified from Peterson *et al.* (1984).

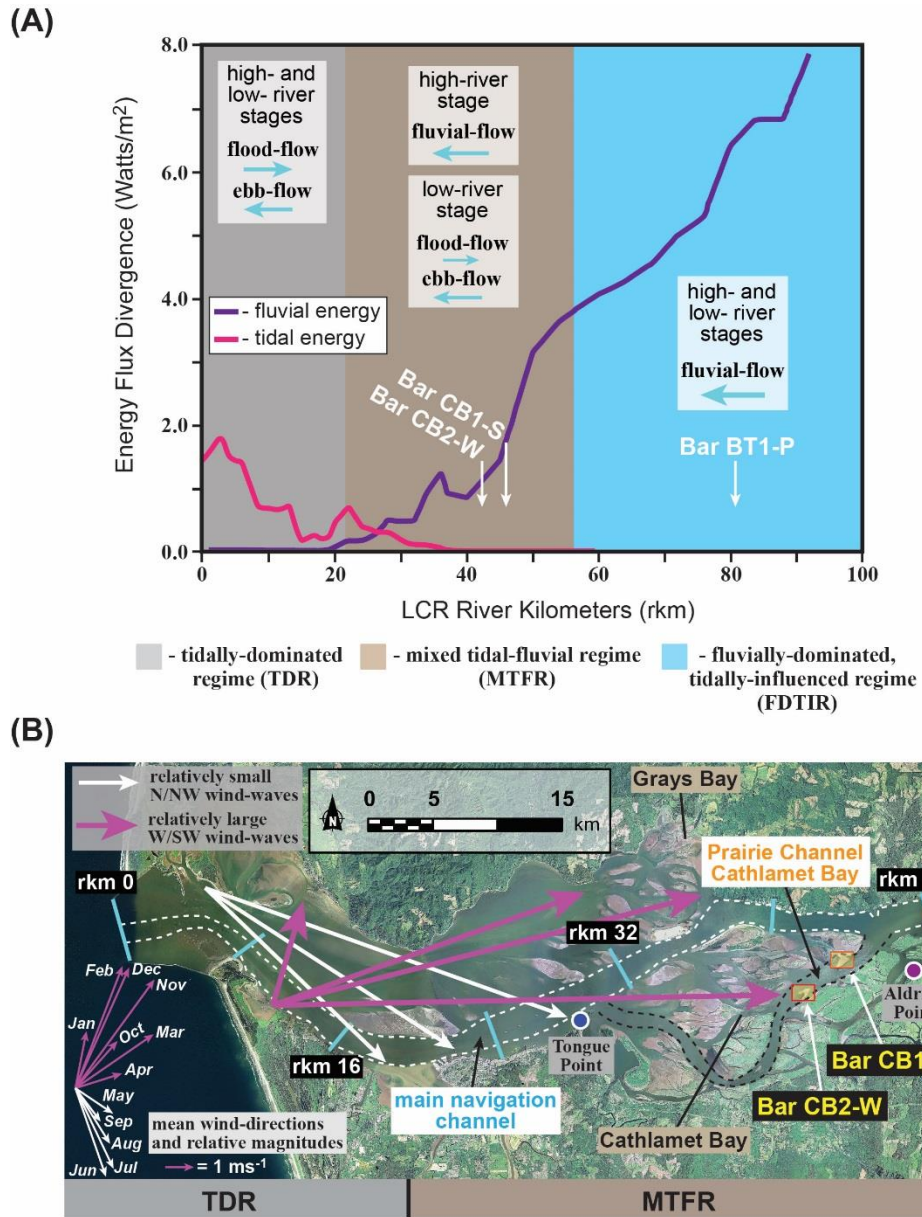


Fig. 4. (A) Mean energy flux divergence of LCR tidal (pink line) vs fluvial (purple line) hydraulic sources as computed by Giese & Jay (1989) and Jay et al. (1990). Note that the summation of tidal- and fluvial-energy fluxes equals the total amount of energy flux across channel cross-sections at each LCR rkm as measured by Jay (1984). (B) Annual LCR intrabasinal wind-wave directions and magnitudes relative to the positions of Bars CB1-S and CB2-W. Note, however, that the image displayed was taken when water-levels were below the Mean Lower Low Water (MLLW) mark, and that the normal condition is for almost all barforms displayed to be submerged when the water surface is higher than MLLW (see figure 6.1, Prokocki *et al.*, 2015). The largest wind-waves (pink arrows) are generated over the longest fetch length between January-April and in October and November, and are oriented from the west-southwest to east-northeast, whilst smaller wind-waves (white arrows) are produced from May to September, and are oriented from north-northwest to south-southeast. Wind data from Peterson *et al.* (2014).

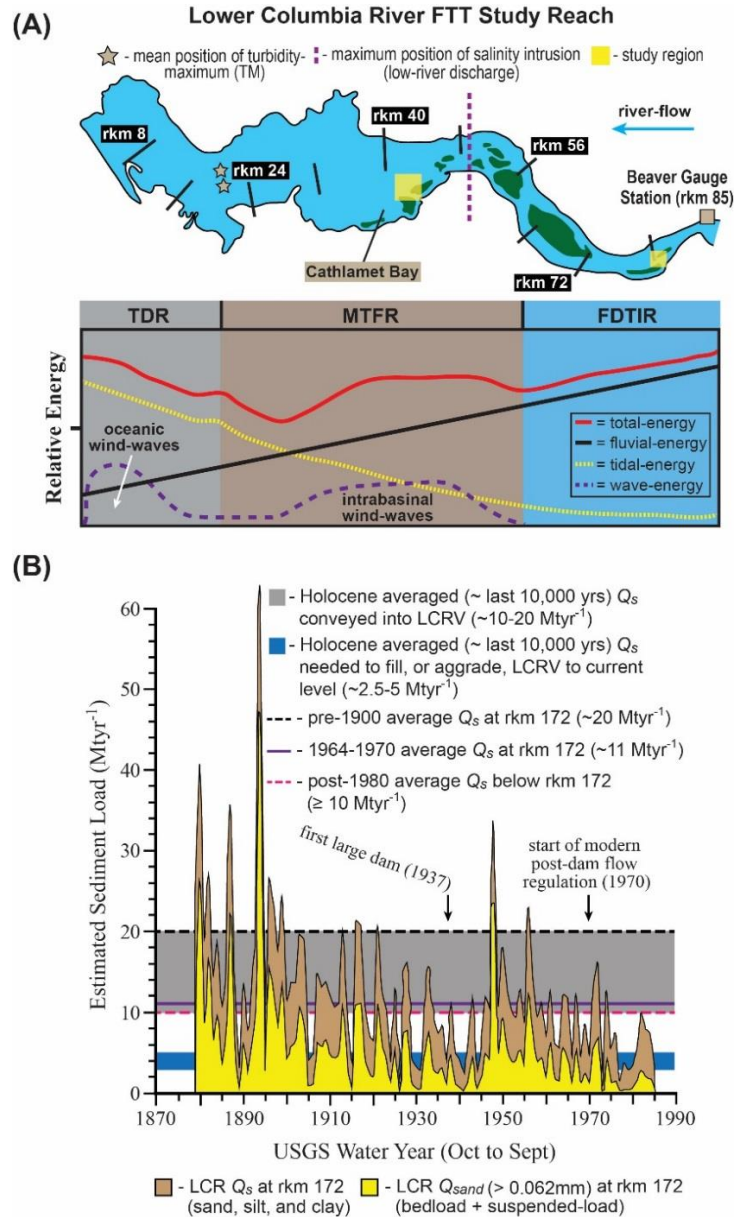


Fig. 5. (A) Temporally averaged relative energy diagram for the LCR FTT study reach investigated. The MTFR (Bars CB1-S and CB2-W) is mainly subjected to fluvial-currents during moderate- to high- river stages, but at low-river stage will experience combined-flows composed of fluvial- and/or tidal- currents and intrabasinal wind-wave oscillatory-currents. Next, within the FDTIR (Bar BT1-P), sediment transport is primarily dictated by fluvial-currents as the result of moderate- to high- river stages. This diagram is based from the results of Jay *et al.* (1990) and Peterson *et al.* (2014). (B) Hindcast estimates (1879-1985) of LCR mean annual sediment load (Q_s), and sand fraction ($Q_{sand} > 0.062\text{mm}$), at rkm 172 given by the discharge- Q_s rating-curve of Sherwood *et al.* (1990). Note that these estimates exclude the sediment contributions of the Willamette and Cowlitz Rivers. Also provided are the: i) Holocene averaged (\sim last 10,000 yrs) estimates of LCR Q_s conveyed to the lower Columbia River Valley (LCRV; grey rectangle) and amount utilized to fill the LCRV to its present level (blue rectangle), and ii) estimations of the pre-1900 (black dashed line), 1964-1970 (purple line), and post-1980 (pink dashed line) LCR Q_s . Modified from Sherwood *et al.* (1990).

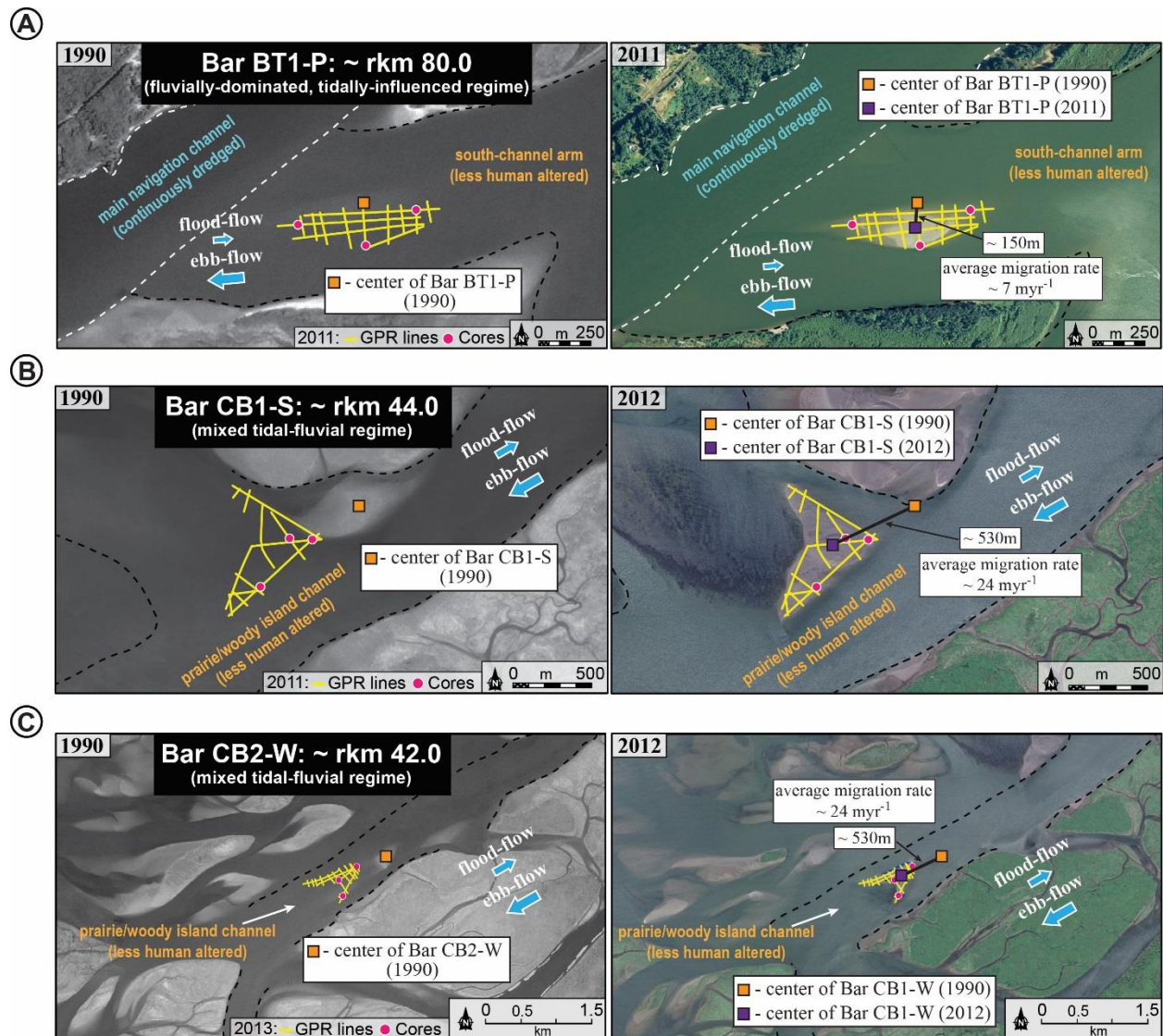


Fig. 6. (A-C) Time sequenced aerial imagery displaying the initial development of Bars BT1-P, CB1-S, and CB2-W, in 1990, and their subsequent migration patterns to 2011/2012, relative to GPR-profiles (yellow lines) and vibracores (pink circles) collected in 2011 (Bars BT1-P and CB1-S) and 2013 (Bar CB2-W), respectively. Reported average migration rates were estimated over the time period 1990-2011 (Bar BT1-P), and 1990-2012 (Bars CB1-S and CB2-W). Note that average migration rates represent the measured straight line distance between the 1990 centre of each bar and its new centre position in 2011, or 2012. Thus, average migration rates are not partitioned into their lateral- and longitudinal- oriented components of translation, and represent overall spatio-temporal movement. Lastly, all bars investigated formed within less human affected secondary channels located away from the consistently dredged main navigation channel (see also Fig. 2 for channel and bar locations). Aerial imagery from US National Agriculture Imagery Program (NAIP) at <https://gdg.sc.egov.usda.gov/>.

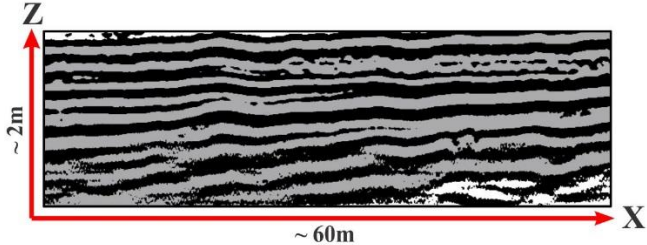
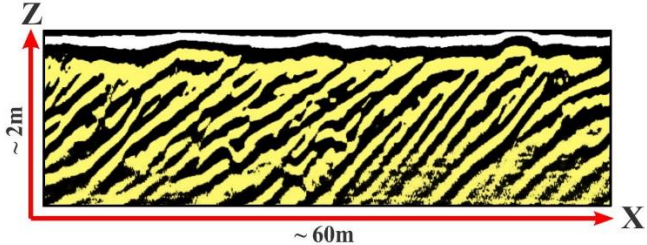
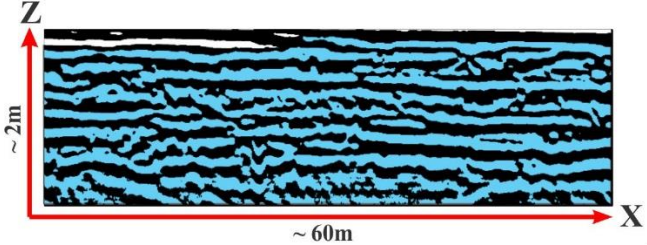
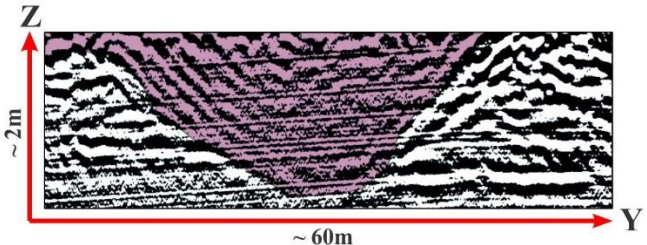
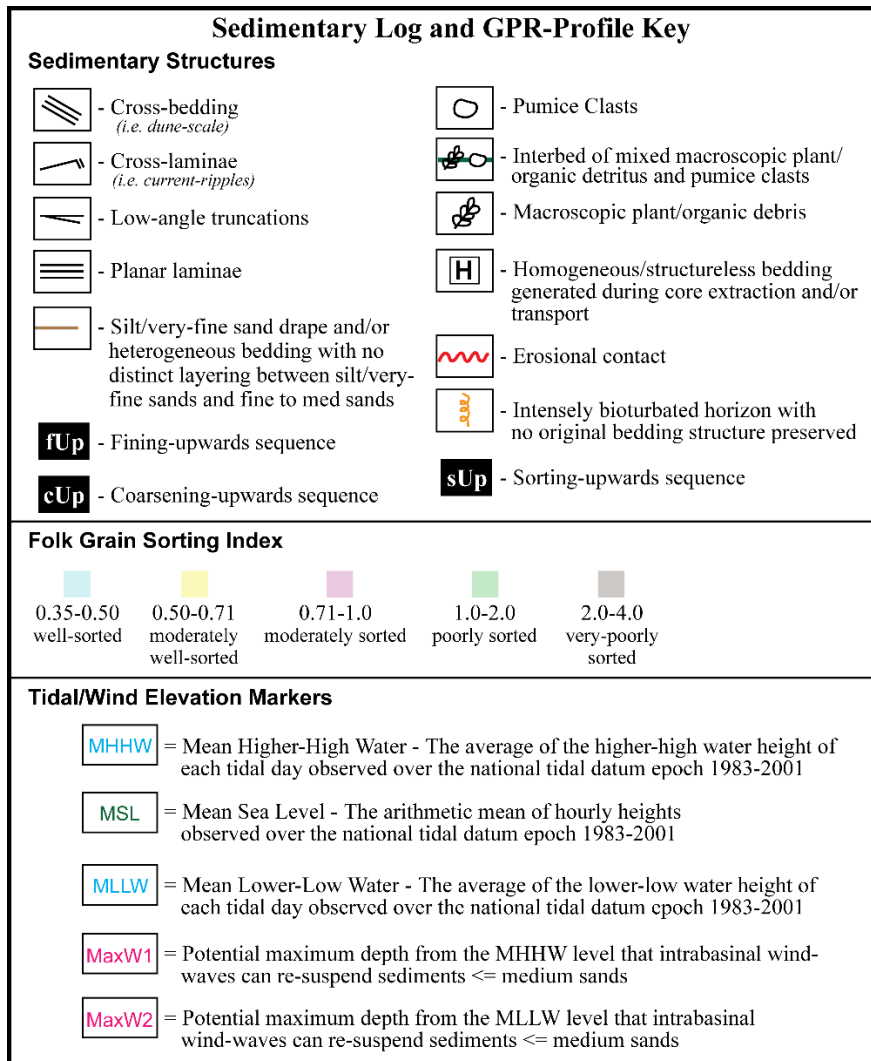
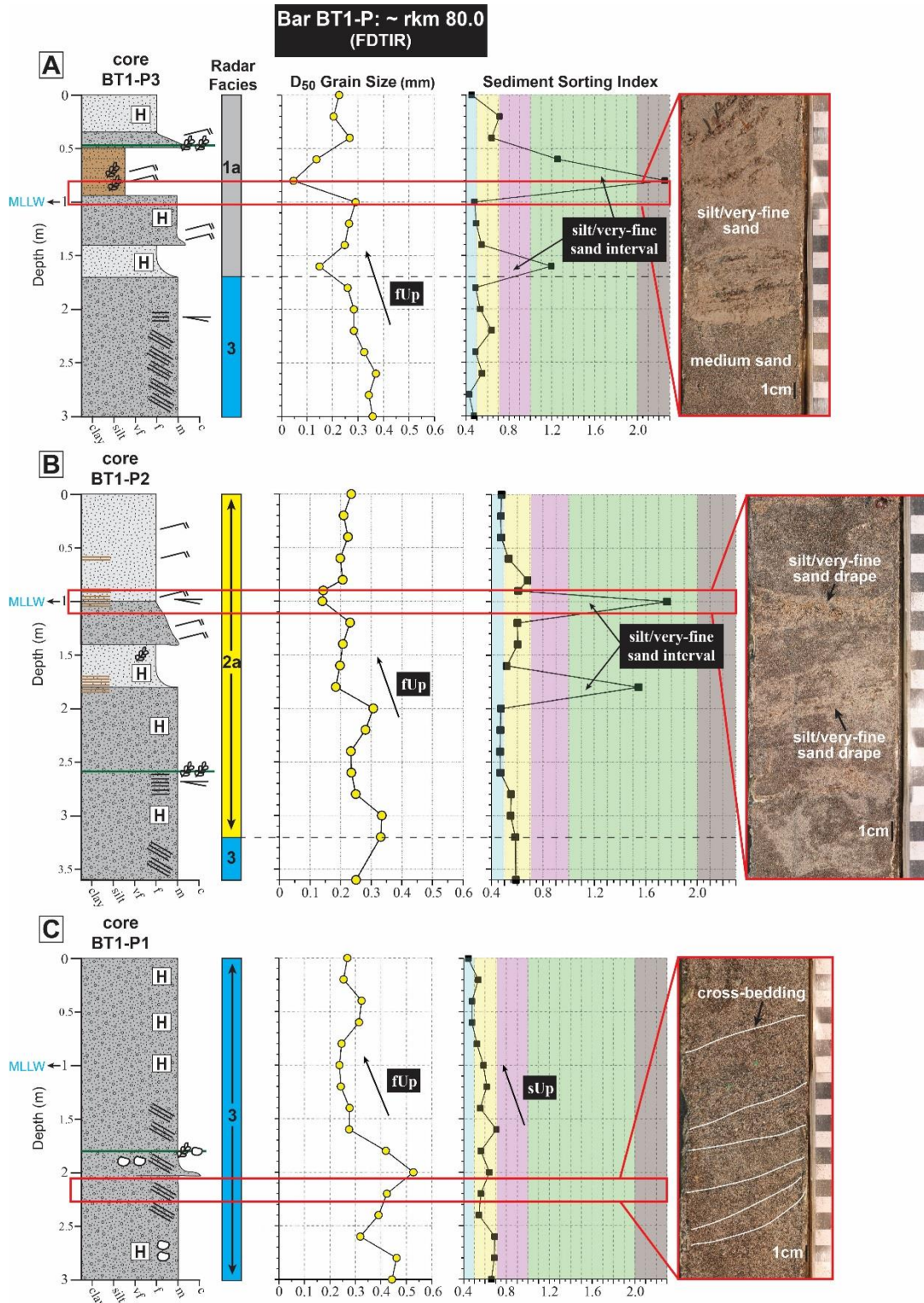
| Radar facies | Facies description | Facies scale | Facies examples |
|--------------|--|--|---|
| 1 | Upper-subtidal to intertidal vertically stacked, laterally- and longitudinally-continuous, low-angle ($< 5^\circ$, but typically $1-2^\circ$) reflectors with high amplitude. Commonly forms near bar-tops (0-5m depth). | Up to 4-5m thick, and can extend to ≤ 500 m in longitudinal (x) and lateral (y) directions |  |
| 2 | Subtidal to intertidal laterally- or longitudinally- continuous sets of high-angle inclined reflectors that are $> 6^\circ$, but are commonly $< 20^\circ$. This facies tends to grade laterally or longitudinally into facies 1 or 3, and may display a range of dip-angles and amplitudes. | Commonly 1-2m thick, but can be up to 4m in thickness, and extends $\sim 30-100$ m in x- or y- directions |  |
| 3 | Mainly subtidal, but can be intertidal, vertically stacked undular, discontinuous, or chaotic, reflectors inclined at $< 6^\circ$. However, parallel reflectors commonly bound the base and tops of trough-shaped reflectors of varying thicknesses and dip-angles. | Stacked-sets can be up to 8m thick, but individual sets are usually 0.25-1m thick. May extend 100s m in x- and y- directions |  |
| 4 | Typically intertidal, but can be subtidal, concave reflectors, with vertically stacked reflectors of variable dip within. This facies always has a strong concave reflector at its base that adjacent reflectors terminate against. | Usually ~ 4 m thick, but can be minimally 1-2m in thickness, and extends 20-100m in y- direction |  |

Table 2. General ground penetrating radar (GPR) reflector facies descriptions and examples captured in LCR mid-channel barform profiles. See main text for specific FTT hydraulic regime sedimentological descriptions and interpretation.

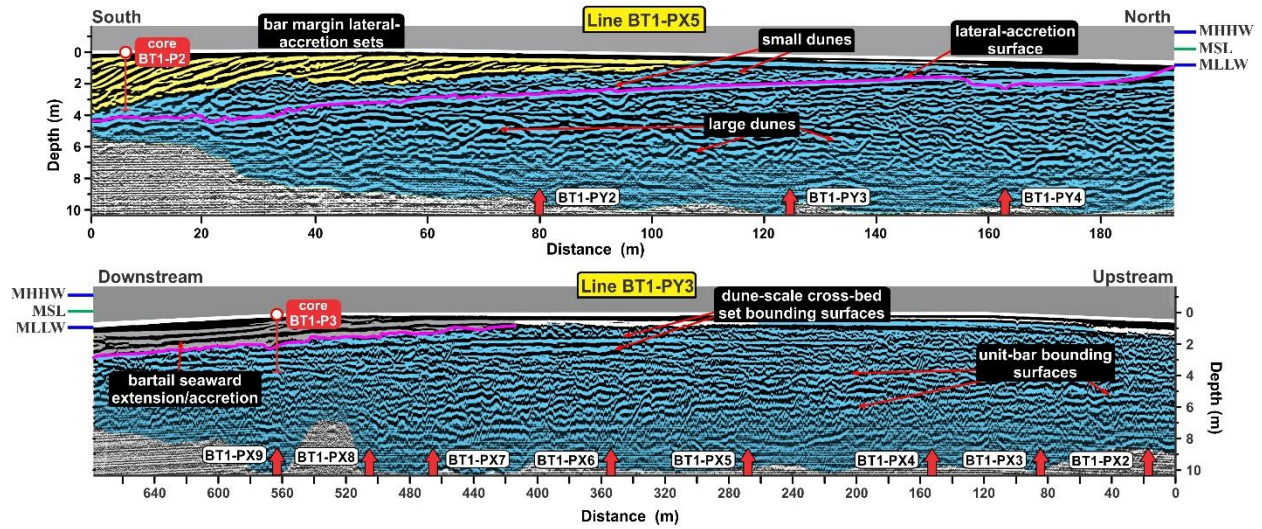
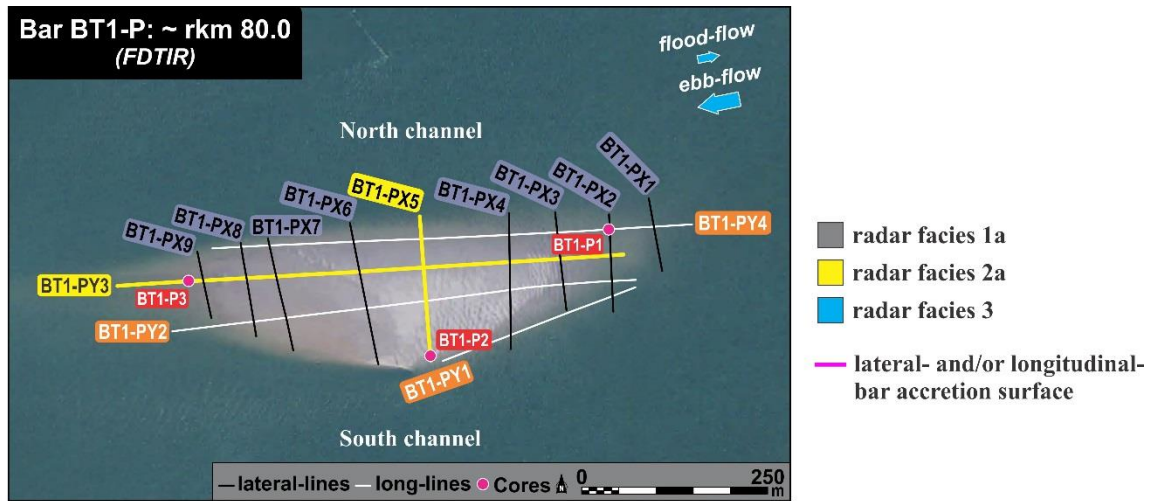


2
3
4
5
6
7
8
9
10
11

Table 3. Key to vibrocore sedimentary logs and GPR cross-sectional profiles. The Mean Higher-High Water (MHHW), Mean Sea Level (MSL), and Mean Lower-Low Water (MLLW) levels displayed on each log and GPR-profile were determined from Stolz *et al.* (2005). Note that the potential maximum depths of LCR intrabasinal wind-wave sediment resuspension (MaxW1 and MaxW2) are from Peterson *et al.* (2014).

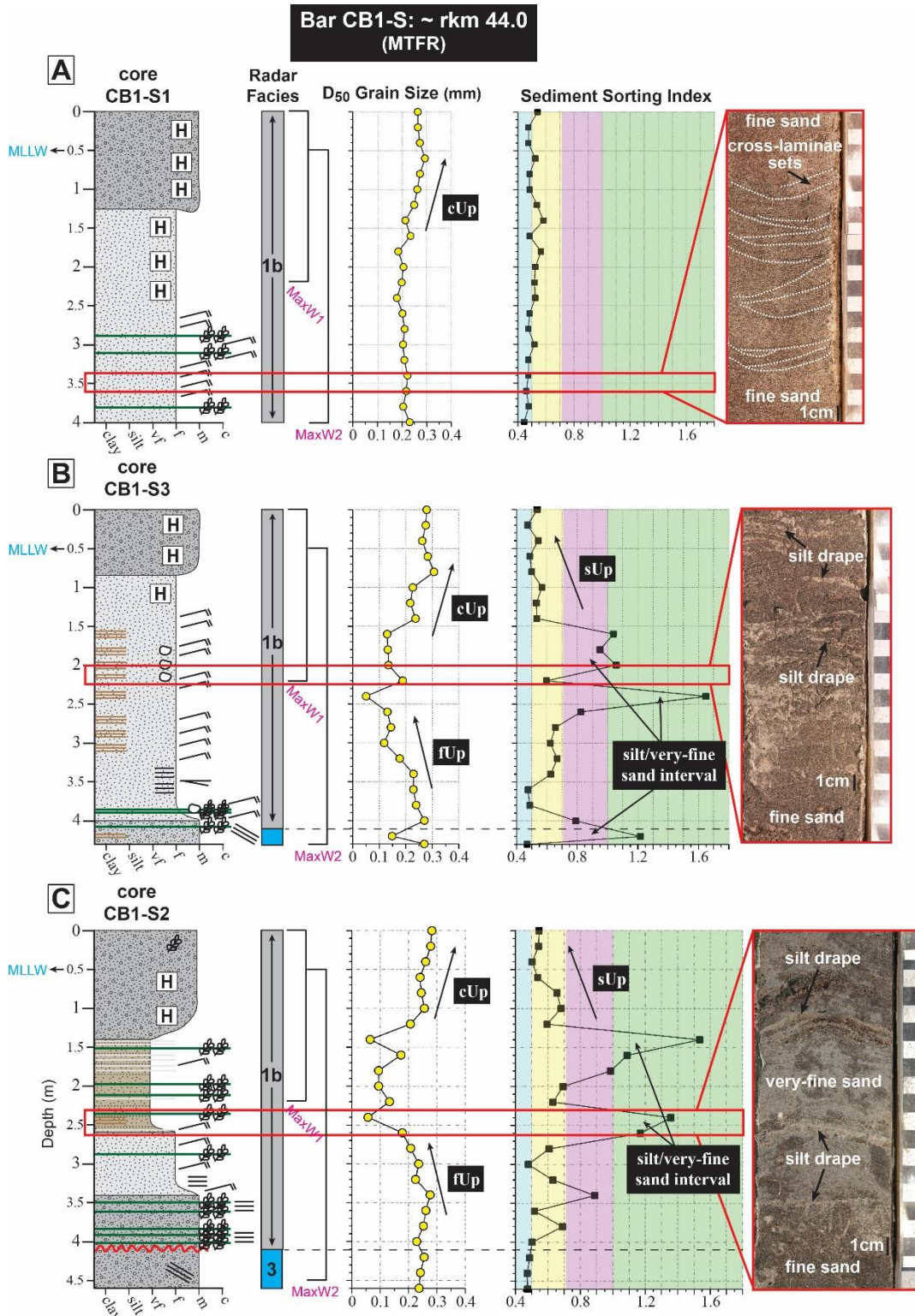


12
 13 Fig. 7. Sedimentary logs, and vertical D_{50} grain size and sediment sorting index trends, of the three
 14 vibracores collected from Bar BT1-P. Cores are presented from downstream (bartail; core BT1-P3) to
 15 upstream (barhead; core BT1-P1). Also marked are the depth intervals that represent the sedimentology
 16 and depositional fabric of coupled radar facies. See Table 3 for key to core logs, and Figure 8 for
 17 locations of vibracores.



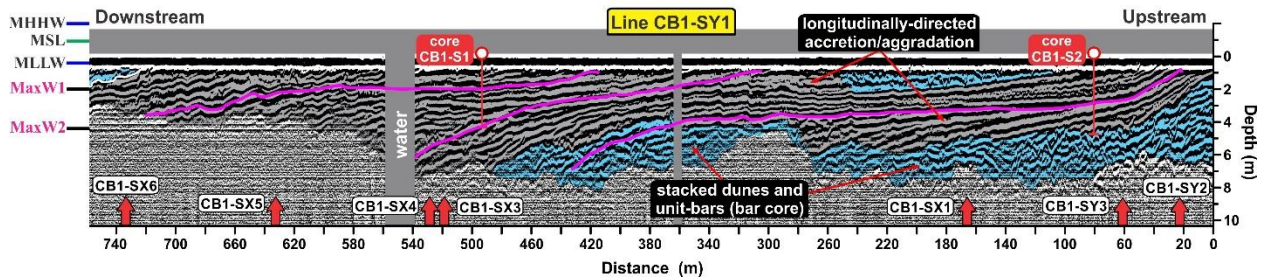
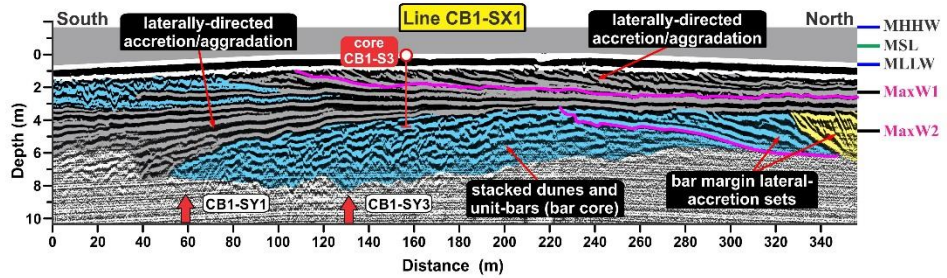
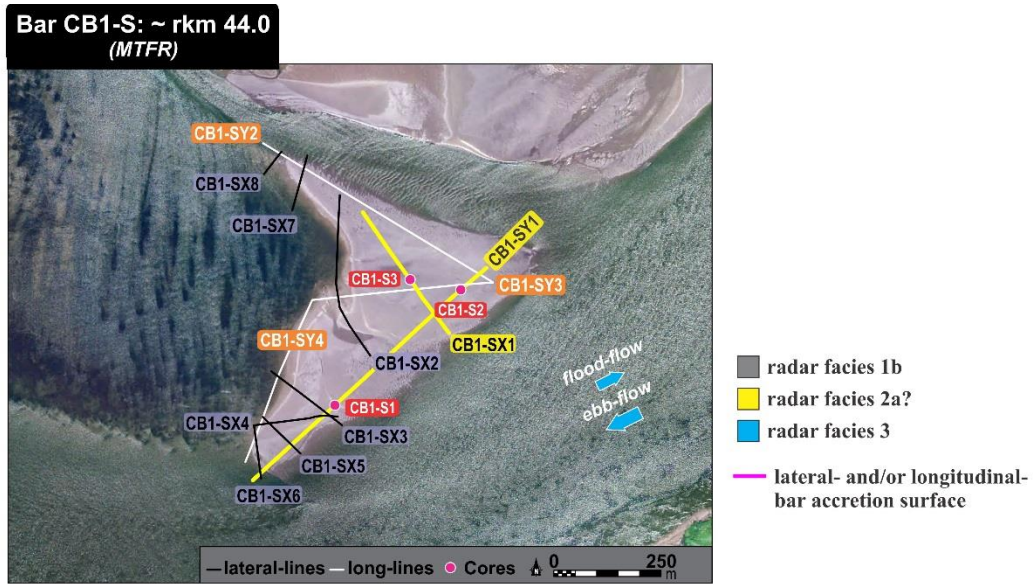
18
19
20
21
22
23
24
25
26
27
28
29
30
31
32
33
34
35

Fig. 8. Interpreted GPR-profiles from Bar BT1-P positioned within the FDTIR. Profiles display the alluvial architecture of Bar BT1-P as formed via the three major radar facies (1-3; Table 2) identified in this study. Included are the locations of vibracores collected along each profile (cores BT1-P2 and BT1-P3), and the radar facies whose sedimentology they preserve. Note the overall dominance in the preservation of radar facies 3.



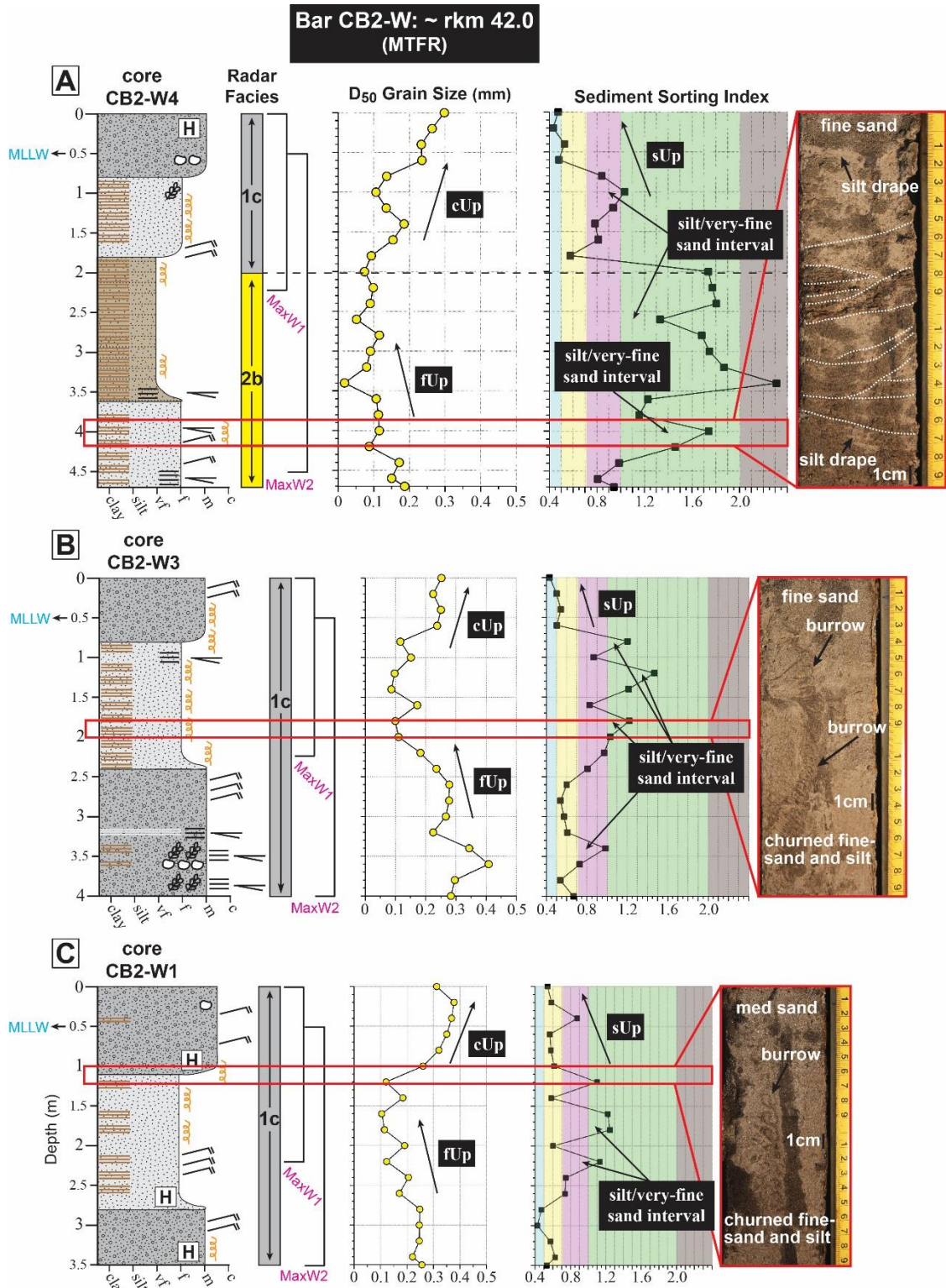
36

37 Fig. 9. Core logs, vertical D_{50} grain size, and sediment sorting index trends, of the three vibracores
 38 collected from Bar CB1-S. Cores are presented from downstream (bartail; core CB1-S1) to upstream
 39 (barhead; core CB1-S2). Also demarcated are the depth intervals representing sediments preserved from
 40 associated radar facies, and maximum depth windows of potential wind-wave influence. See Table 3 for
 41 key to logs, and Figure 10 for vibracore locations.



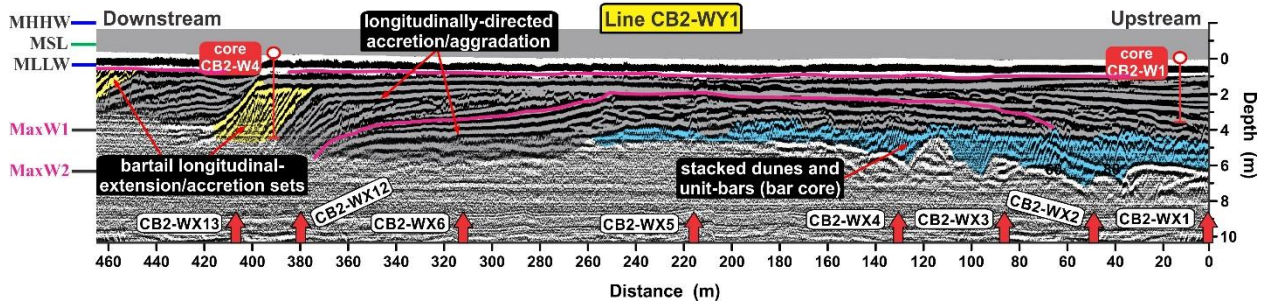
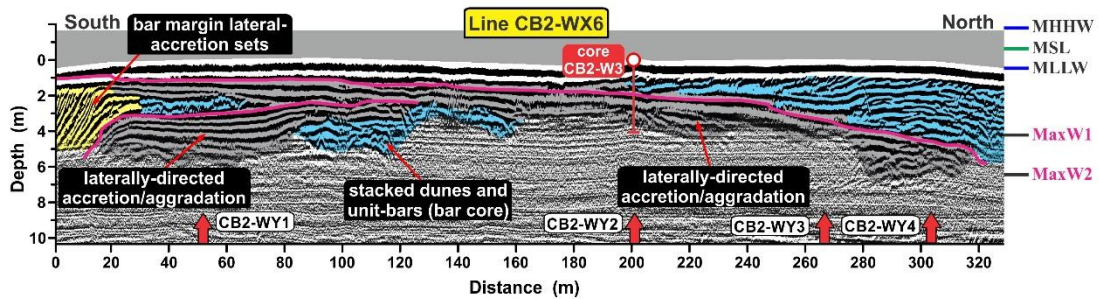
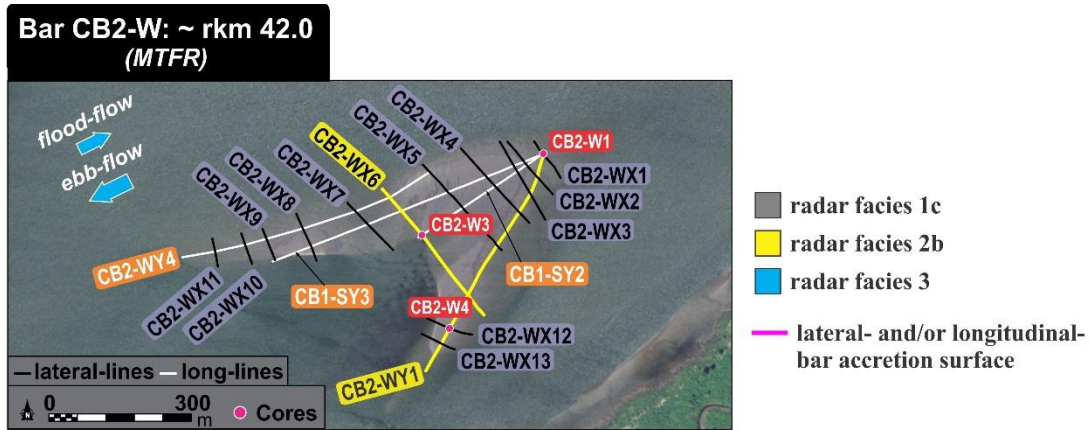
42
43
44
45
46
47
48
49
50
51
52
53
54
55
56
57

Fig. 10. Interpreted GPR-profiles from Bar CB1-S located within the MTFR, which display the alluvial architecture of this bar with respect to preserved radar facies. Also shown are the locations of shallow vibracores collected along each profile (cores CB1-S1, CB1-S2, and CB1-S3), and the radar facies whose sediments they represent. Note the dominant preservation of radar facies 1 and 3.



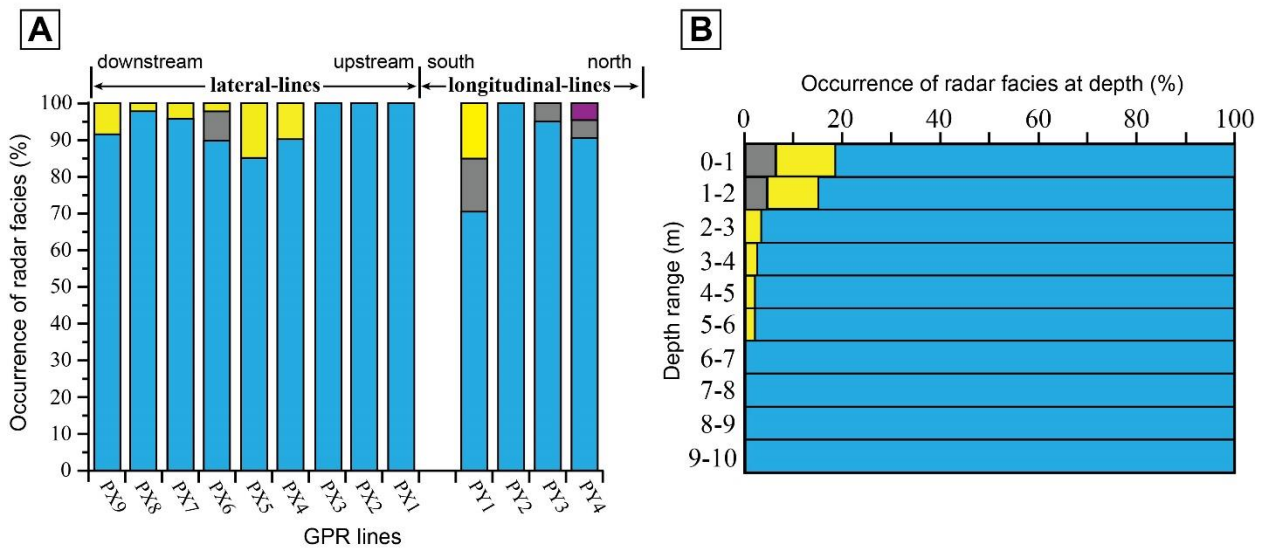
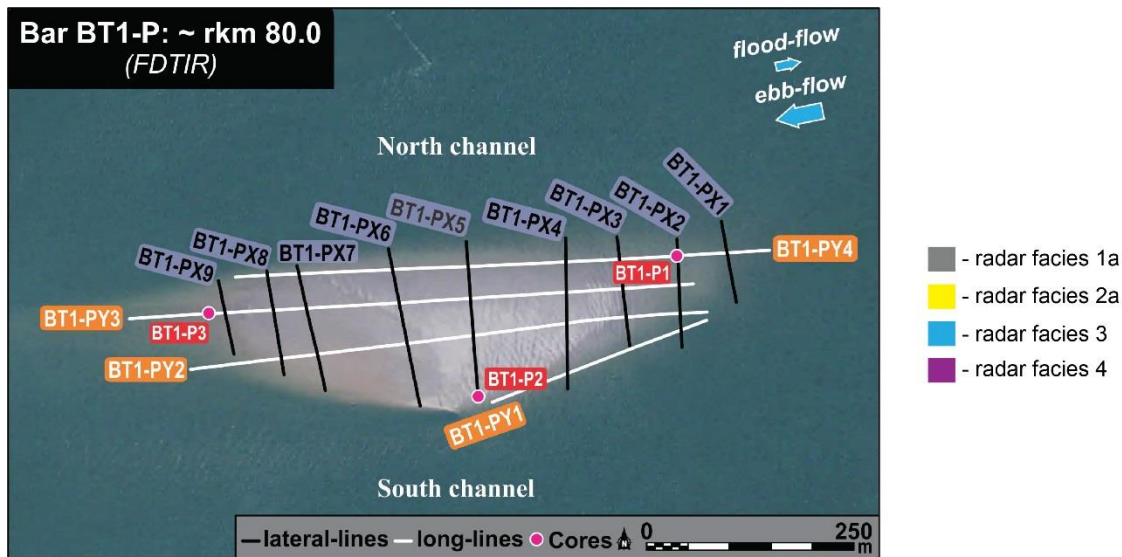
58

59 Fig. 11. Sedimentary logs, vertical D_{50} grain size, and sediment sorting index trends, of the three
 60 vibracores collected from Bar CB2-W. Cores are presented from downstream (bartail; core CB2-W4) to
 61 upstream (barhead; core CB2-W1). Also marked are the depth intervals representing the sedimentology
 62 and depositional fabric of coupled radar facies, and maximum depth windows of potential wind-wave
 63 influence. See Table 3 for key to logs, and Figure 12 for vibracore locations.



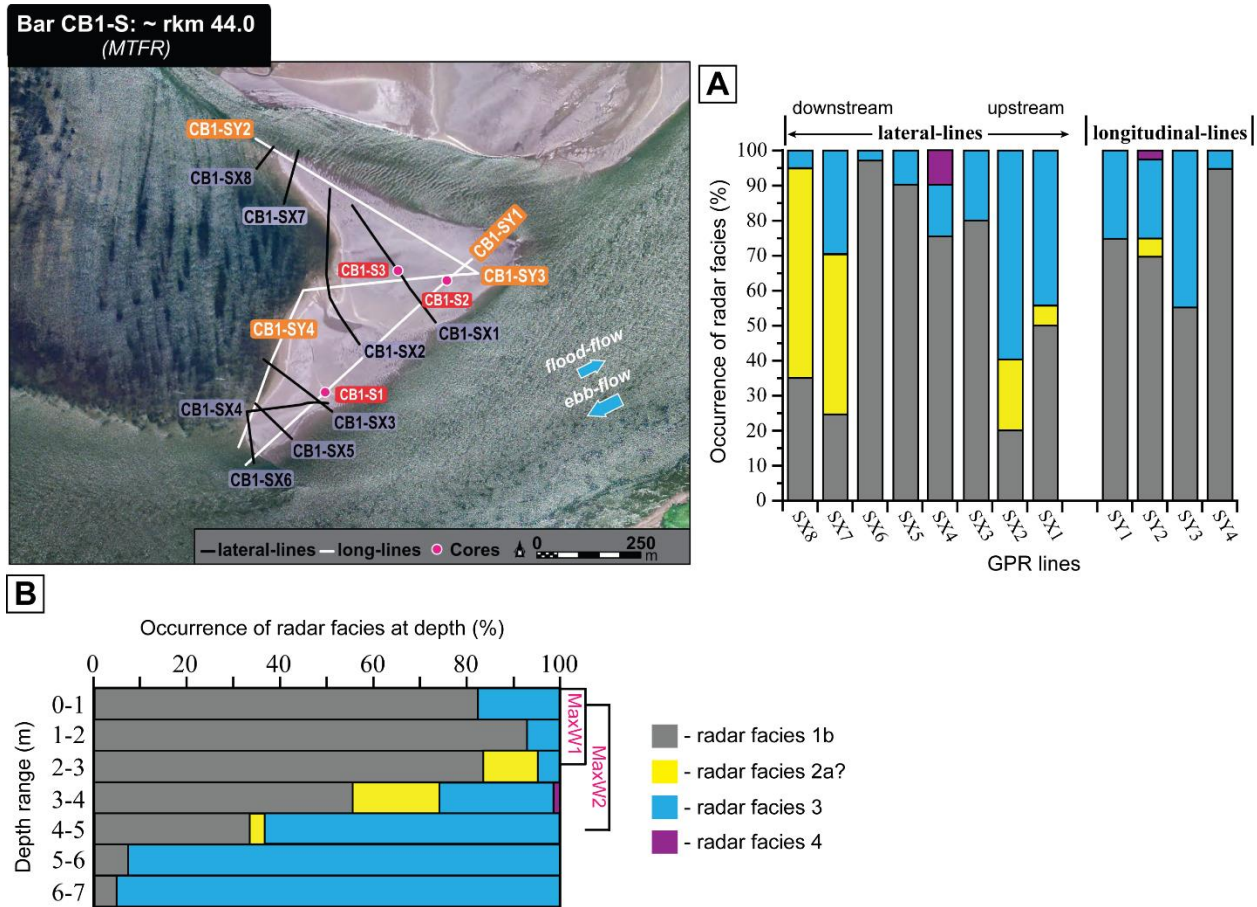
64
65
66
67
68
69
70
71

Fig. 12. Interpreted GPR-profiles from Bar CB2-W positioned within the MTR. Profiles display the preserved stacking patterns of radar facies within Bar CB2-W. Also included are the locations of vibracores collected along each profile (cores CB2-W1, CB2-W3, and CB2-W4), and the radar facies whose sedimentology they preserve. Similar to Bar CB1-S, note the dominant preservation of radar facies 1 and 3.



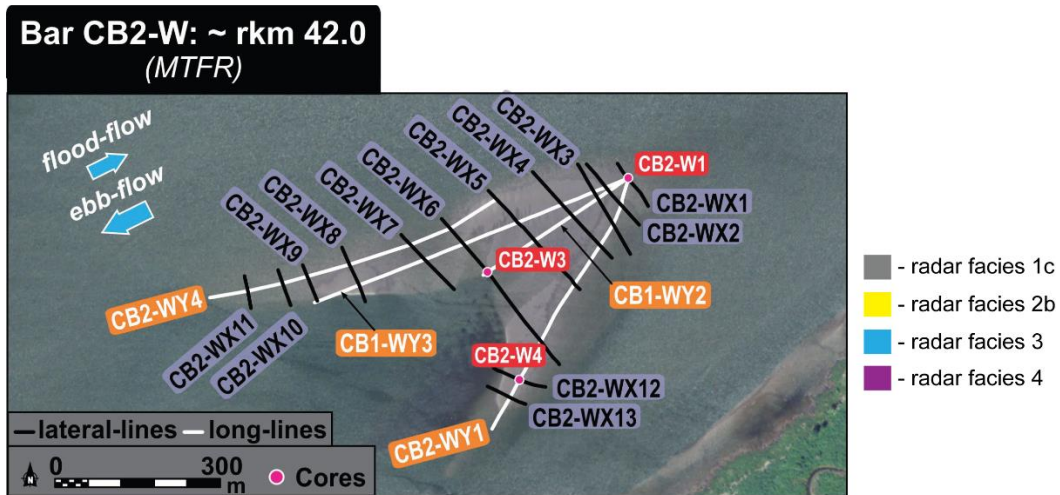
72
73
74
75
76
77
78
79
80
81
82
83
84
85
86
87
88
89

Fig. 13. (A) Areal occurrences of radar facies within each of the thirteen GPR-transects from Bar BT1-P. This bar is dominated by the occurrence of facies 3 with minimal occurrences of facies 1a and 2a. The occurrences of facies 1a is nearly always constrained to bar-tail downstream-extension (lines PY1, PY3, and PY4), whilst the occurrence of facies 2a is mainly confined to bar-margin lateral-accretion (lines PX4-PX9). (B) Calculated occurrences of radar facies within Bar BT1-P GPR-transects with respect to depth. Notice the domination of facies 3 throughout all depth intervals.

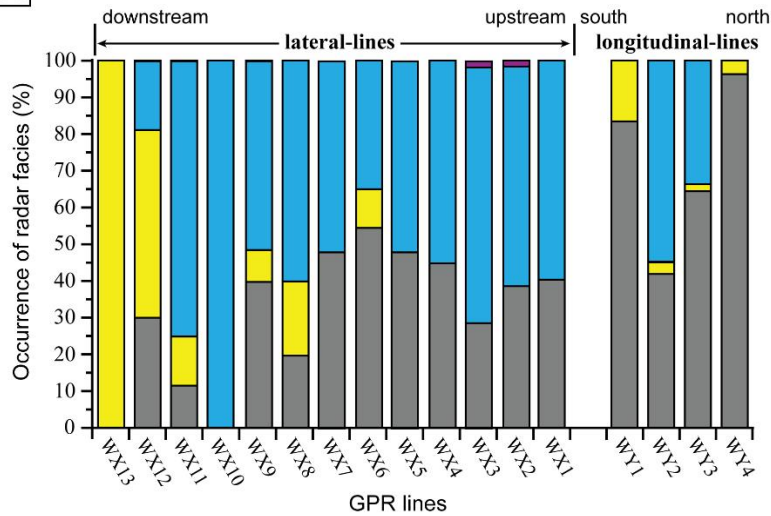


90
91
92 Fig. 14. (A) Spatial distributions of radar facies areal occurrences within the twelve GPR-profiles
93 collected at Bar CB1-S. This bar is dominated by the occurrence of facies 1b, with notable occurrences of
94 facies 2a and 3. Preservation of facies 2a is typically restricted to bar-margin lateral-accretion (lines SX1,
95 SX2, SX7, and SX8), whereas facies 3 is found in variable occurrences within all longitudinal- and
96 lateral- transects. (B) Computed occurrences of Bar CB1-S radar facies with respect to depth. Note that
97 the preservation of facies 3 dominates from 4-7m depth ($\geq 60\%$; below potential wind-wave influence),
98 whilst between 0-4m depth (within potential wind-wave influence) the occurrence of facies 1b ($\geq 55\%$)
99 dominates as the occurrences of facies 2a and 3 diminish to $< 25\%$.

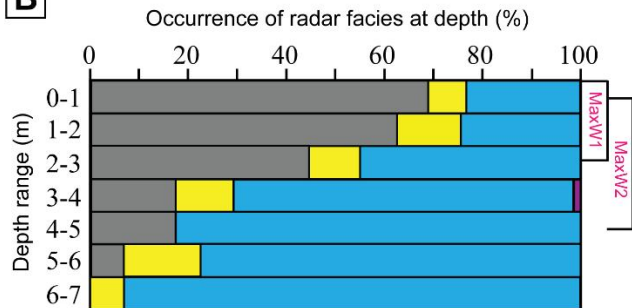
100
101
102
103
104



A

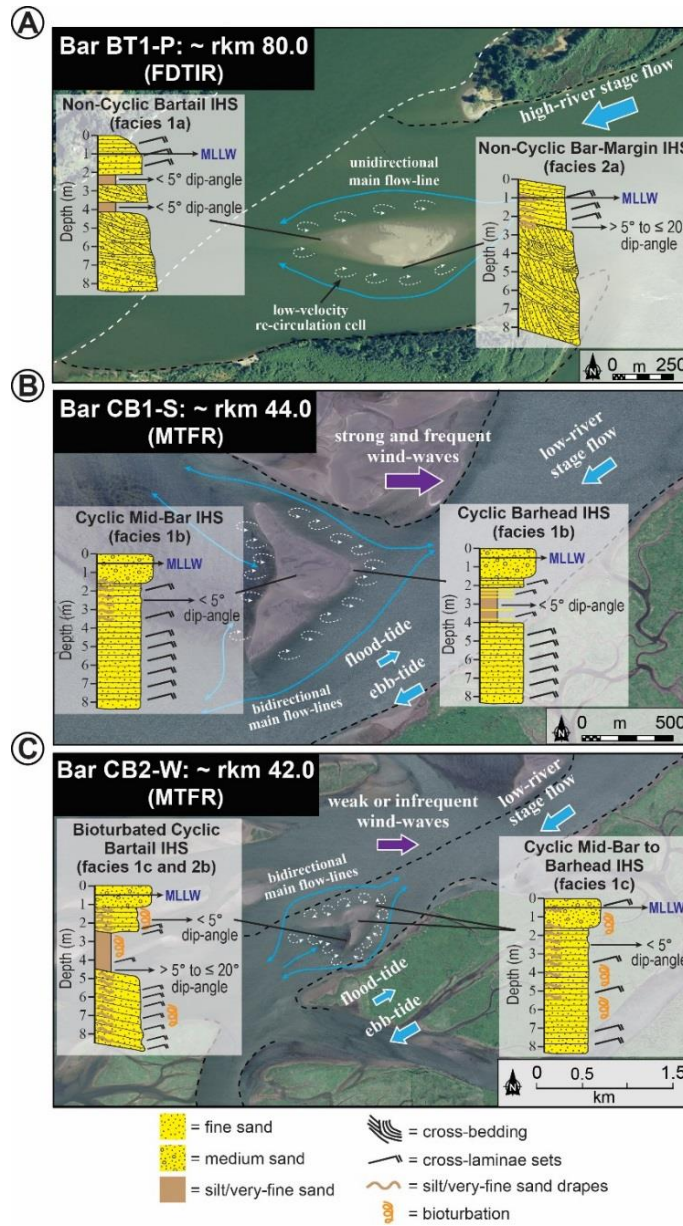


B



105
106

107 Fig. 15. (A) Areal occurrences of radar facies within the seventeen GPR-transects at Bar CB2-W. This bar
108 is primarily composed of facies 1c, 2b and 3, with lower preservation of any style of facies 1 relative to
109 Bar CB1-S. Note that occurrences of facies 2b represent: i) bar-margin lateral-accretion (lines WX6,
110 WX8, WX9, and WX11-WX13), and ii) downstream-oriented bartail-limb accretion (lines WY1 and
111 WY4). (B) Bar CB2-W radar facies occurrences with respect to depth. Notice also that the preservation of
112 facies 3 dominates from 3-7m depth ($\geq 70\%$), whereas between 0-2m depth (within shallowest zone of
113 potential wind-wave influence) the occurrence of facies 1c ($\geq 60\%$) dominates as the occurrence of facies
114 3 diminishes to $< 30\%$. However, unlike at Bar CB1-S, facies 2 (in the form of 2b) is more abundant (~ 8-
115 15% in occurrence) within the 0-3m depth interval.



117

118

119 Fig. 16. Schematic representations of the different styles, depositional fabrics, and positions, of preserved

120 IHS within LCR FTT mid-channel barforms experiencing differing hydraulic processes and sediment

121 transport conditions. (A) IHS is formed primarily during high-river stage events when LCR suspended-

122 sediment concentrations are highest, where fines can be trapped, and deposited, within side-bar and

123 bartail low-velocity recirculation cells. (B) IHS is produced by the redistribution of fines (especially

124 bartail fines) deposited during high-river stage(s) by frequent strong wind-waves + bidirectional tidal-

125 currents at low-river stages. Ebb-tidal currents may carry wind-wave induced resuspended-fines

126 downstream, whilst flood-tidal currents and associated slackwater periods may transport and deposit

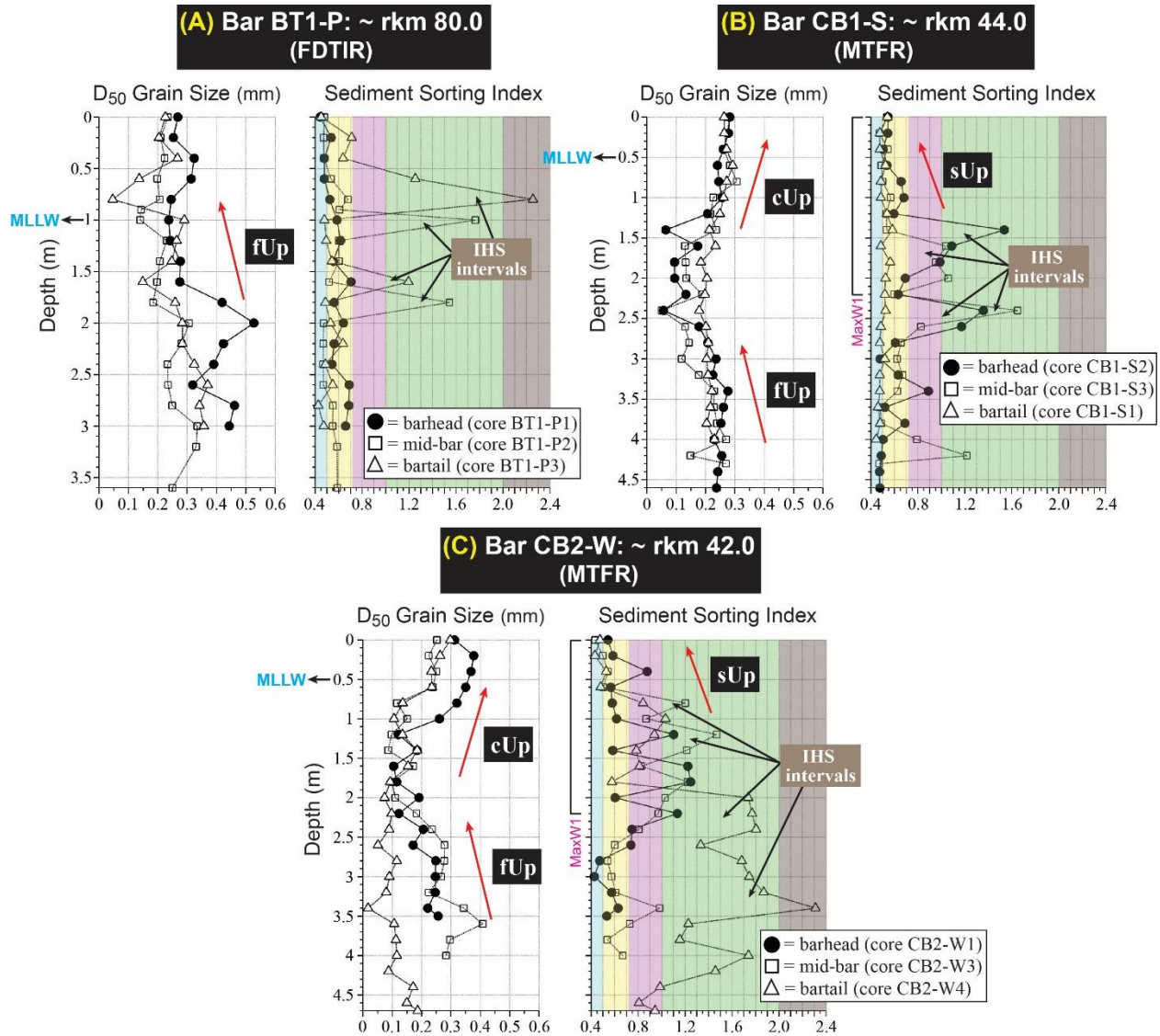
127 wind-wave induced resuspended-fines into mid-bar and barhead accretion-sets. (C) Bartail IHS forms

128 during high-river stage(s) in same method as (A), but during low-river stage, more infrequent weaker

129 wind-waves do not resuspend as many fines, which allows for IHS production from bartail to barhead that

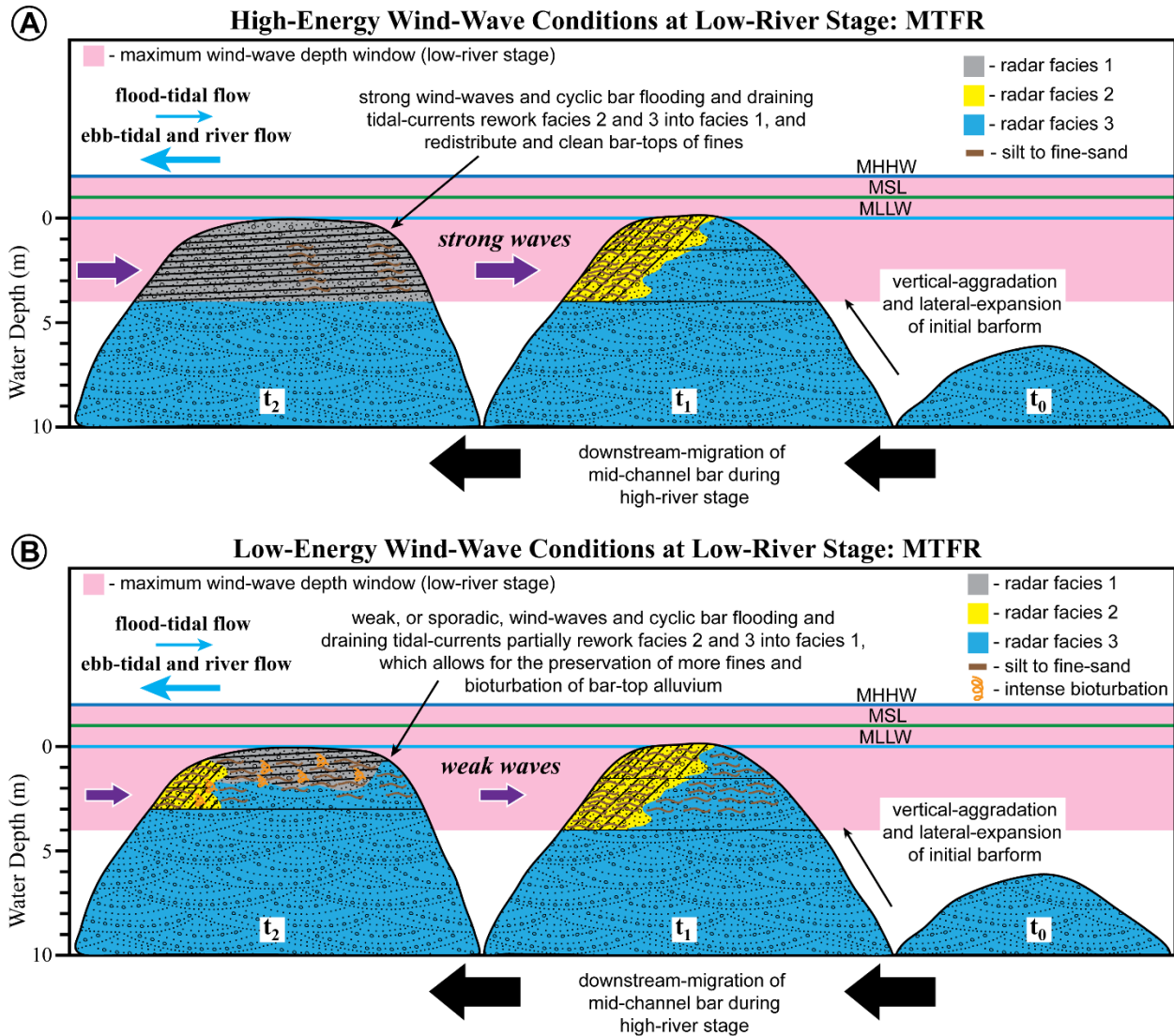
130 is derived from a combination of high river-stage deposited fines and those deposited during tidal

131 slackwater intervals. Note that all IHS within (C) is bioturbated due to weaker wind-wave energy.



132
 133
 134
 135
 136
 137
 138
 139
 140
 141
 142
 143

Fig. 17. Plots of barhead to bartail vibracore D_{50} grain size and sediment sorting trends for the three LCR mid-channel barforms analysed. (A) Bar BT1-P (FDTIR) displays a fining-upwards trend from its barhead to bartail. (B) Bar CB1-S (MTFR) barhead to bartail deposits fine-upward then coarsen- and sort-upward within MaxW1 at ~ 1.5m depth. (C) Bar CB2-W (MTFR) barhead to bartail alluvium fine-upward then coarsen-upward at ~ 1m depth, but do not sort-upward until near the top of MaxW1 at ~ 0.5m depth. See Table 3 for the definitions of abbreviated labels and sediment sorting classifications.



144
 145
 146
 147
 148
 149
 150
 151
 152
 153

Fig. 18. (A) Time sequenced schematic diagram in longitudinal cross-sectional view depicting the architectural and sedimentological evolution of a LCR barform within the MTR that is affected by strong intrabasinal wind-waves during low-river stage. (B) Time sequenced schematic diagram in longitudinal cross-sectional view displaying the architectural and sedimentological evolution of a LCR barform within the MTR that is weakly, or sporadically, influenced by intrabasinal wind-waves during low-river stage.